

# Comparison of multiwavelength observations of 9 broad-band pulsars with the spectrum of the emission from an extended current with a superluminally rotating distribution pattern

H. Ardavan,<sup>1</sup> A. Ardavan,<sup>2</sup> J. Singleton,<sup>3</sup> J. Fasel,<sup>4</sup> W. Junor,<sup>5</sup>  
J. Middleditch,<sup>6</sup> M. R. Perez,<sup>7</sup> A. Schmidt,<sup>4</sup> P. Sengupta,<sup>3,8</sup> P. Volegov<sup>9</sup>

<sup>1</sup>*Institute of Astronomy, University of Cambridge, Madingley Road, Cambridge CB3 0HA, UK*

<sup>2</sup>*Clarendon Laboratory, Department of Physics, University of Oxford, Parks Road, Oxford OX1 3PU, UK*

<sup>3</sup>*MPA-NHMF, MS-E536, Los Alamos National Laboratory, Los Alamos, New Mexico 87545, USA*

<sup>4</sup>*AET-2, MS-E548, Los Alamos National Laboratory, Los Alamos, New Mexico 87545, USA*

<sup>5</sup>*ISR-2, MS-D436, Los Alamos National Laboratory, Los Alamos, New Mexico 87545, USA*

<sup>6</sup>*CCS-3, MS-B265, Los Alamos National Laboratory, Los Alamos, New Mexico 87545, USA*

<sup>7</sup>*Astrophysics Division, 3Y28, NASA Headquarters, 330 E. Street SW, Washington DC 20546, USA*

<sup>8</sup>*T-4, T-CLNS, MS-B258, Los Alamos National Laboratory, Los Alamos, New Mexico 87545, USA*

<sup>9</sup>*P-21, MS-D454, Los Alamos National Laboratory, Los Alamos, New Mexico 87545, USA*

June 2009

## ABSTRACT

The observed spectra of 9 pulsars for which multiwavelength data are available from radio to  $X$ - or  $\gamma$ -ray bands (Crab, Vela, Geminga, B0656+14, B1055-52, B1509-58, B1706-44, B1929+10, and B1951+32) are compared with the spectrum of the radiation generated by an extended polarization current whose distribution pattern rotates faster than light *in vacuo*. It is shown that by inferring the values of two free parameters from observational data (values that are consistent with those of plasma frequency and electron cyclotron frequency in a conventional pulsar magnetosphere), and by adjusting the spectral indices of the power laws describing the source spectrum in various frequency bands, one can account *quantitatively* for the entire spectrum of each pulsar in terms of a single emission process. This emission process (a generalization of the synchrotron-Čerenkov process to a volume-distributed source in vacuum) gives rise to an oscillatory radiation spectrum. Thus, the bell-shaped peaks of pulsar spectra in the ultraviolet or  $X$ -ray bands (the features that are normally interpreted as manifestations of thermal radiation) appear in the present model as higher-frequency maxima of the same oscillations that constitute the emission bands observed in the radio spectrum of the Crab pulsar. Likewise, the sudden steepening of the gradient of the spectrum by  $-1$ , which occurs around  $10^{18} - 10^{21}$  Hz, appears as a universal feature of the pulsar emission: a feature that reflects the transit of the position of the observer across the frequency-dependent Rayleigh distance. Inferred values of the free parameters of the present model suggest, moreover, that the lower the rotation frequency of a pulsar, the more weighted towards higher frequencies will be its observed spectral intensity.

**Key words:** radiation mechanisms: non-thermal—pulsars: individual: Crab pulsar, Vela pulsar, Geminga pulsar, PSR B0656+14, PSR B1055-52, PSR B1509-58, PSR B1706-44, PSR B1929+10, PSR B1951+32.

## 1 INTRODUCTION

Pulsars are unique in emitting a radiation whose spectrum extends from radio waves to gamma rays with essentially the same characteristics (Lyne & Graham-Smith 2006). The

fact that in many pulsars the pulses emitted over widely separated frequency bands (e.g. in the radio and  $X$ -ray bands) are closely aligned in phase and have correlated profiles (Moffett & Hankins 1996; Kuiper et al. 2001, 2002;

Cusumano et al. 2003; Lommen et al. 2007) indicates that both the mechanism by which such pulses are generated and the magnetospheric site from which they originate must be the same for all frequencies. This notwithstanding, the extant models of pulsar radiation invoke a diverse set of unrelated emission mechanisms and emission sites to account for the observational data on multiwavelength characteristics of this radiation (Ruderman & Sutherland 1975; Caraveo et al. 2004; Zavlin 2007; Harding et al. 2008).

It was shown in Ardavan et al. (2008a) that the rigid rotation of the overall distribution pattern of the pulsar emission can only arise from an emitting current whose distribution pattern likewise rotates rigidly with the same angular frequency (see also Section 2). The fact that this requires the pattern of distribution of the emitting current to move with a linear speed exceeding the speed of light *in vacuo* outside the pulsar's light cylinder is not incompatible with special relativity: the charge separation resulting from the coordinated motion of an aggregate of charged particles gives rise to a polarization current whose distribution pattern can have a superluminal motion (Ginzburg 1972; Bolotovskii & Ginzburg 1972; Bolotovskii & Bykov 1990). Moreover, Maxwell's equations show that a polarization current contributes towards the radiation field in just the same way as a current of free charges. In fact, such superluminal sources of radiation have been experimentally realized by several groups (Bessarab et al. 2004; Singleton et al. 2004; Ardavan et al. 2004b; Bolotovskii & Serov 2005).

Here we show that the spectrum of the emission from a polarization current whose distribution pattern rotates faster than light *in vacuo* fits the spectra of 9 pulsars, for which multiwavelength data are available, over the entire range of their output from radio waves to gamma rays. The model we adopt for the source is a generic one: it has an azimuthally-fluctuating distribution pattern that both rotates and oscillates [as realized in recent experiments (Singleton et al. 2004; Ardavan et al. 2004b)], and it has sharp spatial fluctuations in the direction parallel to the rotation axis with power-law spectra in various frequency bands [as demanded by recent numerical models of the pulsar magnetosphere that predict the formation of current sheets (Spitkovsky 2006)]. We infer the values of the two adjustable parameters, characterizing the frequencies of temporal and azimuthal fluctuations of the source, from the observational data, and choose the spectral indices of the power laws describing the spectral distribution of the variations of the source parallel to the rotation axis by optimizing the goodness of fit to the data. We shall see that the theoretical spectra thus derived from a single emission process (a process that takes place in a localized region of the magnetosphere just outside its light cylinder) can *quantitatively* account for the data on all nine of these extensively observed pulsars over 15 to 18 orders of magnitude of frequency.

The emission mechanism in question may be regarded as a generalization of synchrotron-Čerenkov process to a volume-distributed source *in vacuo*. Its spectral distribution is described by the square of a Bessel function whose argument exceeds its order, and so has an oscillating amplitude with an algebraic (rather than exponential) rate of decay with frequency (Ardavan et al. 2003). Giving rise to a radiation whose spectrum is oscillatory, it is a mechanism that naturally accounts for (Ardavan et al. 2008a) the occurrence

of the observed emission bands in the dynamic spectrum of the Crab pulsar (Hankins & Eilek 2007).

The unified explanation this mechanism offers for the apparently unrelated features of pulsar spectra in different spectral bands sharply contrasts with the variety of models, proposed in the published literature, which could at best explain each of these features separately (Ruderman & Sutherland 1975; Caraveo et al. 2004; Zavlin 2007; Harding et al. 2008). The bell-shaped peak of the spectrum in the ultraviolet or X-ray bands that is normally attributed to black-body radiation from hot spots in the pulsar magnetosphere (Caraveo et al. 2004), for instance, emerges as a higher-frequency maximum of the same proportionately-spaced oscillations of the spectrum that Hankins & Eilek (2007) have observed in the radio band. Moreover, the decrease in the spectral index of the radiation by  $-1$  that is universally encountered in pulsar spectra around  $10^{18} - 10^{21}$  Hz turns out to arise, not from any changes in the spectral distribution of the source of the radiation, but from a transition through the Rayleigh distance (see Section 3).

This paper is organized as follows. In Section 2.1, we point out why the observational data on pulsars demand that the source of pulsar radiation should have a superluminally rotating distribution pattern. In Section 2.2, we describe the field due to a constituent volume element of such a source, i.e. the Liénard-Wiechert field generated by the superluminal counterpart of synchrotron process (Schmidt et al. 2007; Ardavan et al. 2004a). In Section 2.3, we consider the field arising from the entire volume of the source. We point out how the most efficient parts of a pulsar magnetosphere for the formation of signals detectable at large distances are the thin filaments within the superluminally rotating part of its current distribution pattern that approach the observer with the speed of light and zero acceleration at the retarded time (Ardavan et al. 2007). Because the wave fronts from each such filament form a caustic on which the contributions that are made towards the field over a finite interval of emission time are received during a considerably shorter interval of observation time, we will see that the overall radiation beam generated by a volume source consists of an incoherent superposition of coherent, narrowing subbeams whose intensities diminish as  $R_P^{-1}$ , instead of  $R_P^{-2}$ , with the distance  $R_P$  from their source (Ardavan et al. 2004a). Consequently, the radiation detected at large distances from the pulsar will always be dominated by these subbeams. In Section 3, we fit the multiwavelength observational data on each of the 9 pulsars listed above with the frequency spectrum predicted for a rotating superluminal source; our earlier derivation of the spectrum (Ardavan et al. 2003) is outlined from an alternative point of view in Appendix A. Implications of the inferred values of the parameters of the fitted spectra will be discussed in Section 4, and a summary will be given in Section 5.

## 2 SUPERLUMINAL MODEL OF PULSARS

### 2.1 Observational constraints on the motion of the distribution pattern of the source

The rigid rotation of the overall distribution pattern of the pulsar emission reflects a radiation field  $\mathbf{E}$  whose cylindrical

components depend on the cylindrical coordinates  $(r, \varphi, z)$  and time  $t$  as

$$E_{r,\varphi,z}(r, \varphi, z; t) = E_{r,\varphi,z}(r, \varphi - \omega t, z, t), \quad (1)$$

where  $\omega$  is the rotation frequency of the pulsar. Such a field can only arise from an electric current whose density  $\mathbf{j}$  likewise depends on the azimuthal angle  $\varphi$  in the combination  $\varphi - \omega t$  only:

$$j_{r,\varphi,z}(r, \varphi, z; t) = j_{r,\varphi,z}(r, \varphi - \omega t, z, t) \quad (2)$$

[see Appendixes A and B of Ardavan et al. (2008a)]. This property of the emitting current follows not only from the observational data, but also from the numerical models of the magnetospheric structure of an oblique rotator; it is found that any time-dependent structures in such models rapidly approach a steady state in the corotating frame (Spitkovsky 2006).

Unless there is no plasma outside the light cylinder, therefore, the emitting polarization current distribution in the magnetosphere of a pulsar should have a superluminally rotating pattern for  $r > c/\omega$  (where  $r$  is the radial distance from the axis of rotation and  $c$  is the speed of light *in vacuo*). Such a source is not inconsistent with special relativity, as the charged particles that make up the polarization current distribution need only move relatively slowly (Ginzburg 1972; Bolotovskii & Ginzburg 1972). It has been experimentally verified that such moving charged patterns act as sources of radiation in precisely the same way as any other moving sources of electromagnetic fields (Bessabab et al. 2004; Ardavan et al. 2004b; Singleton et al. 2004; Bolotovskii & Serov 2005).

Many distinctive features of the emission from a superluminal source are illustrated by the radiation from the following generic polarization current whose distribution pattern rotates and oscillates at the same time:  $\mathbf{j} = \partial \mathbf{P} / \partial t$  for which

$$P_{r,\varphi,z}(r, \varphi, z, t) = s_{r,\varphi,z}(r, z) \cos(m\hat{\varphi}) \cos(\Omega t), \quad -\pi < \hat{\varphi} \leq \pi, \quad (3)$$

and  $\hat{\varphi} \equiv \varphi - \omega t$ . Here,  $P_{r,\varphi,z}$  are the components of the polarization  $\mathbf{P}$  in a cylindrical coordinate system based on the axis of rotation,  $\mathbf{s}(r, z)$  is an arbitrary vector function with a finite support in  $r > c/\omega$ ,  $m$  is a positive integer, and  $\Omega$  is an angular frequency whose value differs from an integral multiple of the rotation frequency  $\omega$  [for the significance of this incommensurability requirement, see Appendix A and Ardavan et al. (2003)]. For a fixed value of  $t$ , the azimuthal dependence of the polarization (3) along each circle of radius  $r$  within the source is the same as that of a sinusoidal wave train with the wavelength  $2\pi r/m$  whose  $m$  cycles fit around the circumference of the circle smoothly. As time elapses, this wave train both propagates around each circle with the velocity  $r\omega$  and oscillates in its amplitude with the frequency  $\Omega$ . This is a generic source: one can construct any distribution with a uniformly rotating pattern,  $P_{r,\varphi,z}(r, \hat{\varphi}, z)$ , by the superposition over  $m$  of terms of the form  $s_{r,\varphi,z}(r, z, m) \cos(m\hat{\varphi})$ . It also corresponds to laboratory-based sources that have been used in experimental demonstrations of some of the phenomena described below (Ardavan et al. 2004b; Singleton et al. 2004).

The results reported here are derived from the retarded solution of Maxwell's equations for the above current dis-

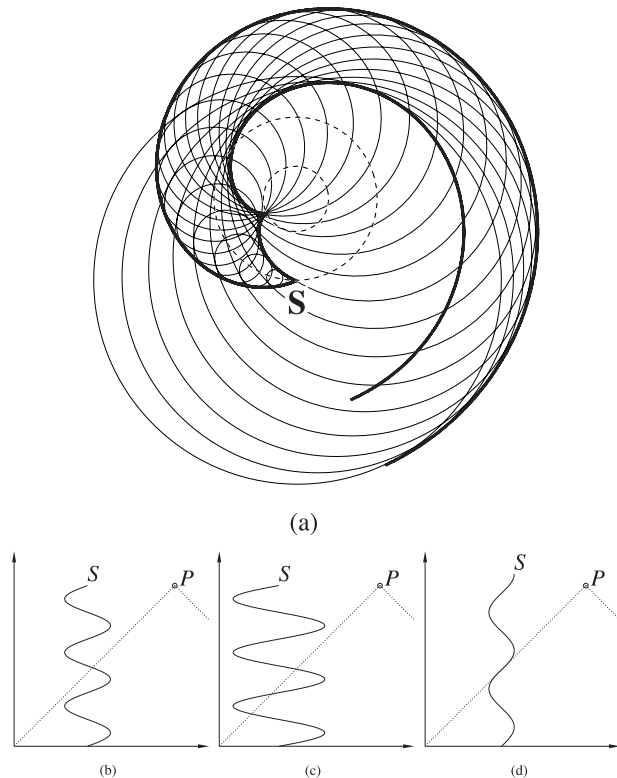


**Figure 1.** (a) Envelope of the spherical wave fronts emanating from a superluminally moving source element (S) in uniform circular motion. The heavy curves show the cross section of the envelope with the plane of the orbit of the source. The larger of the two dotted circles designates the orbit and the smaller the light cylinder. (b), (c) and (d) Space-time ( $ct$  versus  $x$ ) diagrams showing the intersection of the trajectory of the source point  $S$  with the past light cone of the observation point  $P$  when  $P$  lies outside (b), inside (c), and on the cusp of (d) the envelope of wave fronts.

tribution [see Ardavan et al. (2008a, 2007, 2004a, 2003); Schmidt et al. (2007); Ardavan (1998)].

## 2.2 The field generated by a single volume element of the source

A superluminal source is necessarily volume-distributed (Bolotovskii & Ginzburg 1972). However, its field can be built up from the superposition of the fields of its moving constituent volume elements which are essentially point-like. Figure 1(a) shows that the waves generated by a constituent volume element of a rotating superluminal source possess a cusped envelope and that, inside the envelope, *three* wave fronts pass through any given observation point simultaneously. This reflects the fact that the field inside the envelope receives simultaneous contributions from three distinct values of the retarded time [see Fig. 1(c)]. On the cusp of the envelope, where the space-time trajectory of the source is tangent to the past light cone of the observer [Fig. 1(d)], all three contributions toward the value of the field coalesce (Ardavan 1998; Ardavan et al. 2003, 2004a).

On this cusp (caustic), the source approaches the observer with the speed of light and zero acceleration at the re-

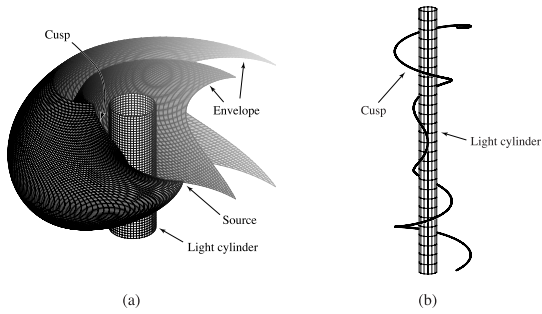


**Figure 2.** Three dimensional views of the envelope (a) and its cusp (b).

tarded time, i.e.  $dR(t)/dt = -c$  and  $d^2R(t)/dt^2 = 0$ , where  $R(t) \equiv |\mathbf{x}(t) - \mathbf{x}_P|$  is the distance between the source point  $\mathbf{x}(t)$  and the observation point  $\mathbf{x}_P$ . As a result, the interval of emission time for the signal carried by the cusp is much longer than the interval of its reception time (Ardavan et al. 2003). This essentially instantaneous reception of contributions from an extended period of emission time represents focusing of the radiation in the time domain: a unique effect that has already been demonstrated experimentally (Ardavan et al. 2004b; Singleton et al. 2004).

A three-dimensional view of the envelope of wave fronts and its cusp is shown in Fig. 2. The two sheets of the envelope, and the cusp along which these two sheets meet tangentially, spiral outward into the far zone. In the far zone, the cusp lies on the double cone  $\theta_P = \arcsin[c/(r\omega)]$ ,  $\theta_P = \pi - \arcsin[c/(r\omega)]$ , where  $(R_P, \theta_P, \varphi_P)$  denote the spherical polar coordinates of the observation point  $P$ . Thus, a stationary observer in the polar interval  $\arcsin[c/(r\omega)] \leq \theta_P \leq \pi - \arcsin[c/(r\omega)]$  receives recurring pulses as the envelope rotates past him/her (Ardavan et al. 2007).

Figure 3 shows the radiation field generated by the rotating source element  $S$  on a cone close to the cusp, just outside the envelope. Not only does the spiralling cusp embody a recurring pulse, but the plane of polarization of the radiation swings across the pulse (Schmidt et al. 2007), as in the radio emission received from pulsars (Lyne & Graham-Smith 2006).

As a consequence of the multivaluedness of the retarded time, three images of the source are observable inside the envelope at any given observation time (Fig. 4). The waves that were emitted when the source was at the retarded positions  $I_1$ ,  $I_2$  and  $I_3$  in Fig. 4 are all received simultaneously at the observation point  $P$ . These images are detected as distinct components, or modes, of the emitted radiation (Boltovskii & Bykov 1990).

Field strengths and polarization position angles of the three images (radiation modes) close to the cusp are shown in Fig. 5. Two modes dominate everywhere except in the middle of the pulse. Moreover, the position angles of two of the modes are ‘orthogonal’ and that of the third swings across the pulse bridging the other two. The constructive interference of the emitted waves on the envelope (where two of the contributing retarded times coalesce) and on its cusp (where all three of the contributing retarded times coalesce) gives rise to the divergence of the field of a point-like source on these loci (Ardavan 1998). Here we plot the spatial distribution of the field excising the narrow regions in which the

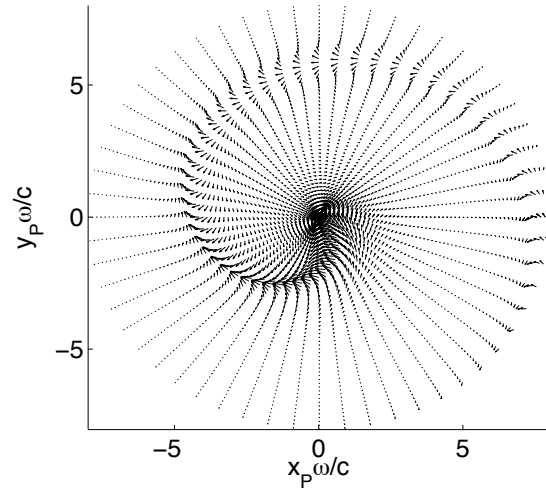


**Figure 3.** Polarization position angles and field strengths on the cone  $\theta_P = \pi/12$  outside the envelope of wave fronts for a source element with  $r\omega = 2$ . Here, the field vectors are projected onto the plane  $(x_P, y_P)$  of the source’s orbit.

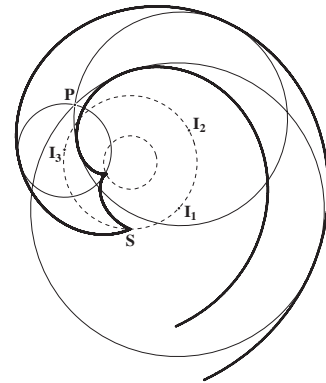


**Figure 4.** An observer  $P$  inside the envelope detects three images ( $I_1$ ,  $I_2$ ,  $I_3$ ) of the source  $S$  simultaneously.

magnitude of the field exceeds a certain threshold (Schmidt et al. 2007).

## 2.3 The field generated by the entire volume of the source

### 2.3.1 Nondiffracting subbeams comprising the overall beam and the nonspherical decay of their amplitudes

The dominant contribution towards the field of an extended source comes from a thin filamentary part of the source that approaches the observer, along the radiation direction, with the speed of light and zero acceleration at the retarded time (Ardavan et al. 2007). For an observation point  $P$  in the far zone with the coordinates  $(R_P, \theta_P, \varphi_P)$ , this filament is located at  $r = (c/\omega) \csc \theta_P$ ,  $\varphi = \varphi_P + 3\pi/2$  and is essentially parallel to the rotation axis (Fig. 6). The collection of cusps of the envelopes of wave fronts that emanate from various volume elements of the contributing filament form a subbeam whose polar width is nondiffracting: the linear dimension of this bundle of cusps in the direction paral-

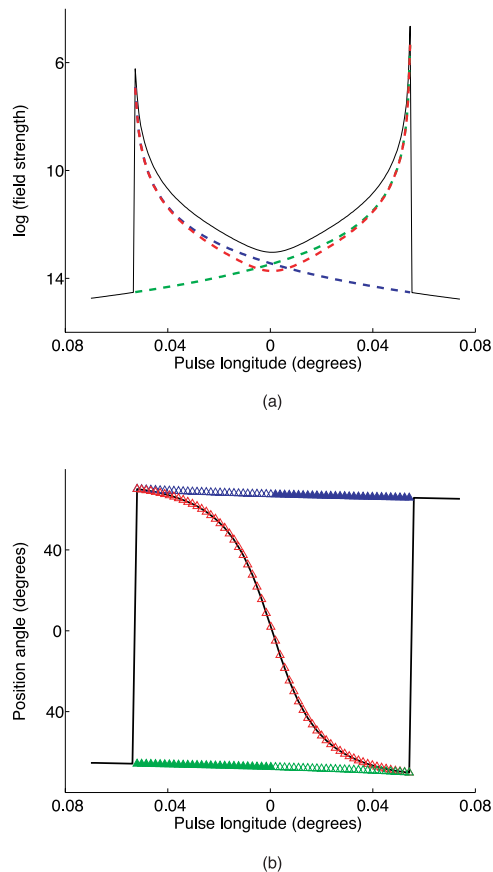


**Figure 5.** (a) The relative strengths of the three radiation modes as observed near the cusp on a sphere of large radius. The total field strength (black) and strengths of the underlying contributions from the three images of the source (green, red, blue) are shown for a source element with  $r\omega = 1.1$  and an observation point that sweeps a small arc of the circle  $R_P\omega/c = 10^{10}$ ,  $\theta_P = \pi/2.7$ , crossing the envelope near the cusp. (b) The corresponding position angles of the contributions from the three retarded times (green, red, blue) are shown relative to one another and to that of the total field (black); the position angles of the dominant contributions are shown with open triangles, and those of the weaker contributions with filled triangles.

parallel to the rotation axis remains the same at all distances from the source, so that the polar angle  $\delta\theta_P$  subtended by the subbeam decreases as  $R_P^{-1}$  with increasing  $R_P$  [Fig. 6 and Ardavan et al. (2007)].

In that it consists of caustics and so is constantly dispersed and reconstructed out of other waves, the subbeam in question radically differs from a conventional radiation beam [see Appendix D of Ardavan (1998)]. The narrowing of its polar width (as  $R_P^{-1}$ ) is accompanied by a more slowly diminishing intensity (an intensity that diminishes as  $R_P^{-1}$  instead of  $R_P^{-2}$  with distance), so that the flux of energy across its cross sectional area remains the same for all  $R_P$  (Ardavan et al. 2007). This slower rate of decay of the emission from a superluminally rotating source has been confirmed experimentally (Ardavan et al. 2004b; Singleton et al. 2004).

The contributing part of an extended source (the filament that approaches the observation point with the speed

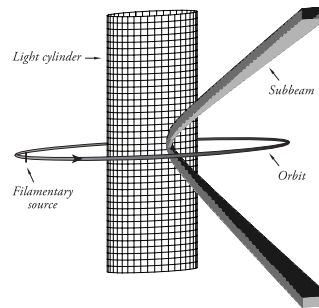


**Figure 6.** Schematic illustration of the light cylinder, the filamentary part of the source that approaches the observation point with the speed of light and zero acceleration at the retarded time, the orbit  $r = c/(\omega \sin \theta_P)$  of this filamentary source, and the subbeam formed by the bundle of cusps that emanate from the constituent volume elements of this filament.

of light and zero acceleration) changes as the source rotates (see Fig. 6). In the case of a turbulent plasma with a superluminally rotating macroscopic distribution, therefore, the overall beam within which the narrow, nonspherically decaying radiation is detectable would consist of an incoherent superposition of coherent, nondiffracting subbeams with widely differing amplitudes and phases [similar to the train of giant pulses received from the Crab pulsar (Słowińska et al. 2005)].

The overall beam occupies a solid angle whose polar and azimuthal extents are independent of the distance  $R_P$ . It is detectable within the polar interval  $\arccos[(r_{<}/\omega/c)^{-1}] \leq |\theta_P - \pi/2| \leq \arccos[(r_{>}/\omega/c)^{-1}]$ , where  $[r_{<}, r_{>}]$  denotes the radial extent of the superluminal part of the source. The azimuthal profile of this overall beam reflects the distribution of the source density around the cylinder  $r = c/(\omega \sin \theta_P)$ , from which the dominant contribution to the radiation arises (Ardavan et al. 2007).

The fact that the observationally-inferred dimensions of the plasma structures responsible for the emission from pulsars are less than 1 metre in size (Hankins et al. 2003) reflects, in the present context, the narrowing (as  $R_P^{-2}$  and  $R_P^{-3}$ , respectively) of the radial and azimuthal dimensions of the filamentary part of the source that approaches the observer with the speed of light and zero acceleration at the retarded time (Ardavan et al. 2007). Not only do the nondiffracting subbeams that emanate from such filaments account for the nanostructure, and so the brightness temperature, of the giant pulses, but the nonspherical decay of the intensity of such subbeams (as  $R_P^{-1}$  instead of  $R_P^{-2}$ ) explains why their energy densities at their source appear to exceed the energy densities of both the plasma and the magnetic field at the surface of a neutron star when estimated on the basis of the inverse square law (Soglasnov et al. 2004).

### 2.3.2 Frequency spectrum of the radiation by a volume source

The spectrum of the radiation emitted by an extended source with a superluminally rotating distribution pattern is oscillatory with oscillations whose spacing increase with frequency [see Ardavan et al. (2008a, 2003) and equation (4) below]. While the Bessel function describing synchrotron

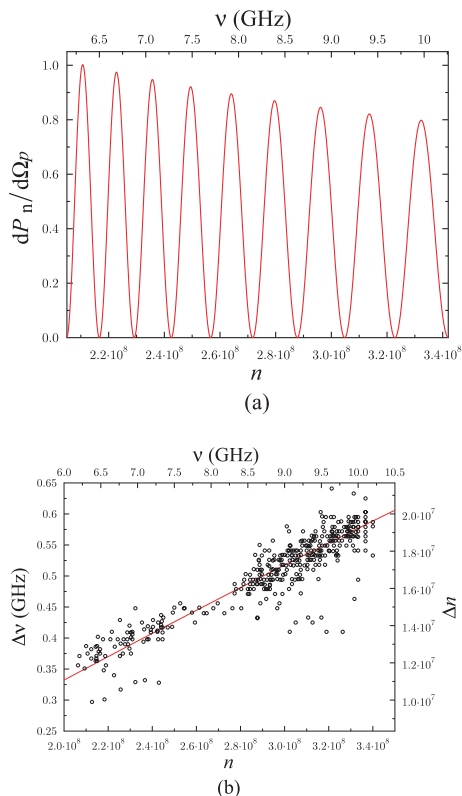


**Figure 7.** The predicted oscillations of the spectrum of the emission for  $\omega/(2\pi) = 30.3$  Hz and  $\Omega/\omega \simeq 1.9 \times 10^4$ , shown in (a), have the same spacing as those of the emission bands in the observed spectrum of the Crab pulsar (Hankins & Eilek 2007), shown in (b) [see Ardavan et al. (2008a)].

radiation has an argument smaller than its order and so decays exponentially with increasing frequency, the Bessel function appearing in the present analysis (Ardavan et al. 2003), whose argument exceeds its order, is an oscillatory function of frequency with an amplitude that decays only algebraically (Abramowitz & Stegun 1970). Figure 7 shows that the spacing of the emission bands in the spectrum of the Crab pulsar fit the predicted oscillations for an appropriate choice of the single parameter  $\Omega/\omega$ . The value of this parameter, thus implied by the data of Hankins & Eilek (2007), places the last peak of the oscillating spectrum at a frequency ( $\sim \Omega^3/\omega^2$ ) that agrees with the position of the ultraviolet peak in the spectrum of the Crab pulsar. By inferring the remaining free parameter  $m$  in equation (3) from the observational data and by adjusting the spectral indices of the power laws describing the spectral decomposition of the source density  $\mathbf{s}$  in various frequency bands [see Section (3)], we are thus able to account for the continuum spectrum of the Crab pulsar over 16 orders of magnitude of frequency (Fig. 8).

At radiation frequencies higher than  $\sim 10^{18}$  Hz, the Rayleigh distance [see Section 3.5 and Brooker (2003)] becomes larger than the distance of the Crab pulsar from the Earth. For an observer within the Rayleigh distance, the emission arises from a narrower radial extent of the source, and so has a higher degree of mean polarization, the higher the frequency. The degree of circular polarization of such a high-frequency emission decreases with increasing frequency

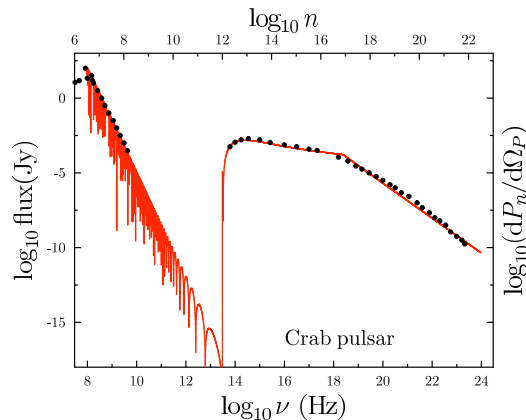


**Figure 8.** The points show observational data (where available) on the spectrum of the Crab pulsar. The curves show the spectral distribution  $\log(dP_n/d\Omega_P)$ , predicted by equations (4), (8) and (9), versus  $\log n$  and  $\log \nu$  for  $\nu = n\omega/(2\pi) \simeq 30.3n$  Hz and  $\Omega/\omega \simeq 1.9 \times 10^4$ . In the model, the recovery of intensity at the ultraviolet peak ( $\sim 10^{15}$  Hz) is caused by resonant enhancement due to the azimuthal modulation frequency  $m\omega/(2\pi) \simeq 3 \times 10^{13}$  Hz. The steepening of the gradient of the spectrum by  $-1$  at  $2.4 \times 10^{18}$  Hz reflects a transition through the Rayleigh distance.

$\nu$  as  $\nu^{-1/3}$ , so that this emission is essentially 100 per cent linearly polarized at all phases, including off-pulse phases [see equation (A26) below]. Note that, in this model, the intensity and polarization of the off-pulse emission, too, reflect the distributions of density and orientation of the emitting current around the cylinder  $r = c/(\omega \sin \theta_P)$  within the pulsar magnetosphere (Ardavan et al. 2007).

We will see in Appendix A that the reason the spectrum of the emission from the source distribution (3) is not limited, in the superluminal case, to just the frequencies  $\Omega \pm m\omega$  is the following. On the one hand, each element  $\hat{\varphi}$  of a constituent ring of the source makes its contribution towards the observed field at the discrete set of retarded times  $\omega t = \varphi_P - \hat{\varphi} + 3\pi/2 + 2k\pi$  at which it approaches the observer with the speed of light and zero acceleration, i.e. *periodically* with the period  $2\pi/\omega$  ( $k$  is an integer). On the other hand, temporal modulations of the density of this source occur on a time scale  $2\pi/\Omega$  that is incommensurable with the period  $2\pi/\omega$ . Because the emission time of the element labelled by  $\hat{\varphi}$  is fixed (via  $\omega t = \varphi_P - \hat{\varphi} + 3\pi/2 + 2k\pi$ ) by its initial azimuthal position ( $\hat{\varphi}$ ), the temporal  $[\cos(\Omega t)]$  and spatial  $[\cos(m\hat{\varphi})]$  modulations of source (3) effectively combine into a single variation  $[\propto \exp(i\Omega\hat{\varphi}/\omega) \cos(m\hat{\varphi})]$ . It is the Fourier decomposition of this variation with  $\hat{\varphi}$ , or equivalently with the retarded time  $t$ , that together with the incommensurability of the two periods ( $2\pi/\omega$  and  $2\pi/\Omega$ ), and the finiteness of the domain of definition of  $\hat{\varphi}$ , results in a spectrum containing all frequencies [see Fig. 5 of Ardavan et al. (2003)].



### 3 THEORETICAL FITS TO THE MULTIWAVELENGTH DATA ON PULSAR SPECTRA

#### 3.1 The equation used to create the fits

Using the result derived in Appendix A [equation A30)], we can write the frequency dependence of the power that is radiated by the source distribution (3) per harmonic per unit solid angle as

$$\begin{aligned} \frac{dP_n}{d\Omega_P} \propto & S_1(n)^2 \text{Ai}^2 \left[ - \left( \frac{2}{n} \right)^{1/3} \frac{\Omega}{\omega} \right] \\ & + S_2(n)^2 \left( \frac{2}{n} \right)^{2/3} \text{Ai}'^2 \left[ - \left( \frac{2}{n} \right)^{1/3} \frac{\Omega}{\omega} \right] \\ & + 2S_3(n)^2 \left( \frac{2}{n} \right)^{1/3} \text{Ai} \left[ - \left( \frac{2}{n} \right)^{1/3} \frac{\Omega}{\omega} \right] \\ & \times \text{Ai}' \left[ - \left( \frac{2}{n} \right)^{1/3} \frac{\Omega}{\omega} \right], \end{aligned} \quad (4)$$

in which

$$S_1(n) = n^{2/3} |K_r| K_{\varphi_0} \left( |\bar{s}_r|^2 + |\bar{s}_\varphi \cos \theta_P - \bar{s}_z \sin \theta_P|^2 \right)^{1/2},$$

$$S_2(n) = n^{2/3} |K_r| K_{\varphi_0} \left( |\bar{s}_\varphi|^2 + |\bar{s}_r|^2 \cos^2 \theta_P \right)^{1/2},$$

and

$$\begin{aligned} S_3(n) = & n^{2/3} |K_r| K_{\varphi_0} \\ & \times \left\{ \Im \left[ \bar{s}_r^* \cos \theta_P (\bar{s}_\varphi \cos \theta_P - \bar{s}_z \sin \theta_P) - \bar{s}_r \bar{s}_\varphi^* \right] \right\}^{1/2}. \end{aligned}$$

Here,  $\bar{s}_{r,\varphi,z}$  are the Fourier components of the source densities  $s_{r,\varphi,z}|_{\hat{r}=\text{csc}\theta_P}$  with respect to  $z$  [see equation (A27)],  $\Im$  and the superscript star denote the imaginary part and the conjugate of a complex variable, respectively, and  $(R_P, \theta_P, \varphi_P)$  are the spherical polar coordinates of the observation point  $P$ . The function  $K_{\varphi_0}$  is defined by

$$K_{\varphi_0} = (-1)^{n+m} \sin \left( \frac{\pi\Omega}{\omega} \right) \left( \frac{\mu_+}{n - \mu_+} + \frac{\mu_-}{n - \mu_-} \right), \quad (5)$$

and the various frequencies involved ( $n$ ,  $\mu_+$ , etc.) are tabulated for convenience in Table 1. Finally, the function  $K_r$  is defined for various frequency ranges in Table 2;  $\hat{r}_<$  and  $\hat{r}_>$  denote the radial boundaries of the part of the source that contributes towards the radiation at  $P$  in units of the light-cylinder radius  $c/\omega$ .

#### 3.2 Fit procedure

The pulsar spectra are fitted to the predicted spectrum (4) by adjusting the modulation frequencies  $\Omega/2\pi$  and  $m\omega/2\pi$  of the source (see Table 1), and by specifying the required rates of change of the Fourier components  $\bar{s}_{r,\varphi,z}$  of the source density (or equivalently, and more practically,  $S_1$ ,  $S_2$  and  $S_3$ ) with frequency  $\nu = n\omega/2\pi$ . Our objective in each case is to illustrate that the observed spectrum can be faithfully represented by that in equation (4) within a wide margin of accuracy. We will model the frequency dependence of the factors that multiply the Airy functions in this equation by as simple a set of power laws as allowed by the available data. We will also extrapolate the spectra thus derived into the frequency intervals for which no data are available.

The position of the peak of the last oscillation in the

**Table 1.** Frequencies involved in the fitting of the pulsar spectra. For convenience in comparisons with observations, most parameters are presented in frequency units (i.e. in Hz) rather than as angular frequencies (i.e. in radians per second).

Frequency	Definition
$\frac{\omega}{2\pi}$	pulsar rotation frequency
$\nu = \frac{n\omega}{2\pi}$	observation frequency
$\frac{m\omega}{2\pi}$	azimuthal modulation frequency
$\frac{\Omega}{2\pi}$	temporal modulation frequency
$\mu_+$	$\frac{\Omega}{\omega} + m$
$\mu_-$	$\frac{\Omega}{\omega} - m$

**Table 2.** Limiting values of parameters and functions in various frequency ranges; the harmonic number  $n$  yields the observation frequency  $\nu = n\omega/2\pi$  in units of the rotation frequency  $\omega/2\pi$ .

Function	Frequency range	Limiting value
$\text{Ai} \left[ - \left( \frac{2}{n} \right)^{1/3} \frac{\Omega}{\omega} \right]$	$n \ll \left( \frac{\Omega}{\omega} \right)^3$	$\left( \frac{2}{n} \right)^{-1/2} \left( \frac{\Omega}{\omega} \right)^{-1/4}$
$\text{Ai} \left[ - \left( \frac{2}{n} \right)^{1/3} \frac{\Omega}{\omega} \right]$	$n \gg \left( \frac{\Omega}{\omega} \right)^3$	$\text{Ai}(0)$
$\text{Ai}' \left[ - \left( \frac{2}{n} \right)^{1/3} \frac{\Omega}{\omega} \right]$	$n \ll \left( \frac{\Omega}{\omega} \right)^3$	$\left( \frac{2}{n} \right)^{1/2} \left( \frac{\Omega}{\omega} \right)^{1/4}$
$\text{Ai}' \left[ - \left( \frac{2}{n} \right)^{1/3} \frac{\Omega}{\omega} \right]$	$n \gg \left( \frac{\Omega}{\omega} \right)^3$	$\text{Ai}'(0)$
$K_{\varphi_0}$	$n \ll \mu_+$	$\sim 1$
$K_{\varphi_0}$	$n \sim m \gg \frac{\Omega}{\omega}$	$\sim n$
$K_{\varphi_0}$	$n \gg \mu_+$	$\sim n^{-1}$
$K_r$	$n \ll \frac{\pi \hat{R}_P}{(\hat{r}_> - \hat{r}_<)^2}$	$\simeq \hat{r}_> - \hat{r}_<$
$K_r$	$n \gg \frac{\pi \hat{R}_P}{(\hat{r}_> - \hat{r}_<)^2}$	$\simeq \left( \frac{2\pi \hat{R}_P}{n} \right)^{1/2} \exp \left( -\frac{i\pi}{4} \right)$

spectrum of the radiation described by equation (4) is determined by the ratio  $\Omega/\omega$ . Observational data specify the value of this ratio for each of the 9 pulsars we consider quite accurately [see also Ardavan et al. (2008a)]. However, the existing data are insufficient to determine the remaining parameters of the source [frequency  $m\omega$  of the azimuthal modulations of the current distribution (3) and the frequency dependence of the Fourier components  $\bar{s}_{r,\varphi,z}$  of the amplitude of this current] uniquely. We will assume that the amplitudes  $\bar{s}_{r,\varphi,z}$  [or equivalently the functions  $S_i(n)$ ,  $i = 1, 2, 3$ , that appear in equation (4)] have power-law dependences of the form  $n^{\alpha_i}$  on the harmonic number  $n$  with differing exponents  $\alpha_i$  in different frequency bands. The relative amplitudes,  $S_2/S_1$  and  $S_3/S_2$ , and the values of  $\alpha_i$  are then inferred from the data.

We start plotting each figure with the inferred values of the above adjustable parameters in the radio band and continue the resulting theoretical curves as far as the next patch of available data for which one or more of these parameters

have different values. In a few cases (Vela, Geminga and B0656+14), we will cover an interval for which no data are available by extrapolating the theoretical curves implied by the data on opposite sides of the empty interval until they meet. We are not predicting that the spectrum would necessarily follow the plotted curves in frequency intervals where no data are available. Not only is the polarization current distribution in the magnetosphere of a pulsar not expected to have such a simple space-time structure as that described by equation (3), but even in such a simplified description, the amplitudes  $\bar{s}_{r,\varphi,z}$  need not have the power-law forms we have approximated them by.

Before embarking on a detailed description of the fits, we show, in the following three Subsections, how the behaviour of the various components of equation (4) (see Table 2) leads to some “universal” features of the emission spectra of pulsars. Evidently, many of the gross phenomena seen in pulsar observations are *quite general consequences* of the fact that they arise from a rotating, superluminal source. It is only in modelling the *detailed behaviour* of the spectra that it is necessary to specify parameters  $S_1$ ,  $S_2$  and  $S_3$  (which represent intricacies of the ‘weather’ around the emitting region as opposed to the ‘climate’ in the pulsar magnetosphere) with any accuracy.

### 3.3 Resonant enhancement

According to equation (5), the value of  $K_{\varphi_0}$  (and, hence, those of  $S_1$ ,  $S_2$  and  $S_3$ ) can undergo a sudden change as a result of the resonance between the radiation frequency  $\omega n/2\pi$  and one of the source frequencies  $\omega\mu_{\pm}/2\pi$ . As summarized in Table 2,  $K_{\varphi_0}$  is independent of  $n$  ( $\sim 1$ ) when  $n \ll \mu_+$ , decays as  $n^{-1}$  when  $n \gg \mu_+$ , and is of the order of  $n$  when  $n \sim m \gg \Omega/\omega$  [see equation(5)]; hence, its value sharply increases by several orders of magnitude for  $n \sim m \gg \Omega/\omega$ . This is the primary cause of the recovery of the intensity at higher frequencies that will be seen in the fitted spectra below.

### 3.4 The Airy function and its derivative

The Anger functions appearing in the general expression for the radiated power [equation (66) of Ardavan et al. (2003)] reduce to Bessel functions for  $n \gg 1$  and to Airy functions for  $n \gg \Omega/\omega$  [see Appendix C of Ardavan et al. (2008a)]. In most parts of the spectra modelled here,  $\Omega/\omega \ll n \ll (\Omega/\omega)^3$  and so  $\text{Ai}'/\text{Ai}$  is greater than unity (Table 2). Consequently, when the second term of equation (4) is employed in the fits below,  $S_2/S_1$  is given values of the order of  $10^6$ . In other words, where invoked, the second term is actually comparable to the first term everywhere apart from the region past the last maximum. The dependence on  $n$  of band spacings and amplitudes of the two functions  $\text{Ai}$  and  $\text{Ai}'$  are sufficiently different for the inclusion of the second term to make a difference to the shape of the spectrum.

The third term of equation (4) declines with  $n$  at a similar rate to the second term in regions of the spectrum where  $n \ll (\Omega/\omega)^3$ . However, it was not found necessary to invoke this term in the fits below, probably because  $S_3$  is much smaller than  $S_1$  and  $S_2$  when the phases of the Fourier components ( $\bar{s}_r, \bar{s}_\varphi, \bar{s}_z$ ) of the source density  $\mathbf{s}$  do not bear

any relationship with one another. Unlike  $S_1$  and  $S_2$  that depend on the absolute values of these (generally complex) quantities,  $S_3$  sensitively depends on their relative phases. In addition, the first two terms are positive for all  $n$ , while the third term oscillates between positive and negative values. Since the measurement of this term by any instrument would entail an integration with respect to frequency over a non-zero bandwidth, these oscillations will likely make the detected value of the third term negligibly smaller than those of  $S_1$  and  $S_2$ .

### 3.5 The Rayleigh distance

The coefficient  $K_r$  changes from being independent of  $n$  to decaying as  $n^{-1/2}$  when  $n$  increases past  $\pi R_P/(\hat{r}_> - \hat{r}_<)^2$  (Table 2). On rearranging this condition for  $n$  in terms of  $R_P$ , we obtain

$$R_P \sim \frac{a^2}{\lambda} \equiv d_R, \quad (6)$$

where  $\lambda = c/\nu$  is the wavelength of the electromagnetic radiation and  $a = r_> - r_<$  is the radial extent of the emitting current. In geometrical optics, the parameter  $d_R$  is known as the *Rayleigh distance* for an aperture or source of linear dimension  $a$ ; it corresponds roughly to the transition between the conditions for Fresnel and Fraunhofer diffraction (Brooker 2003).

Whilst the Rayleigh distance is most frequently encountered in optical or radio experiments when using monochromatic radiation and varying the distance between source and observer (Brooker 2003), here we cross it by keeping  $R_P$  fixed and varying the frequency  $\nu = n\omega/2\pi$ . In the following fits to data, the transition across the Rayleigh distance accounts for the steepening of the observed spectra by the factor  $n^{-1}$  in the X-ray band and enables us to derive the radial extent  $\hat{r}_> - \hat{r}_<$  of the emitting plasma that contributes towards the subpulse detected at the observation point.

Having described the general behaviour of equation (4), we now embark on the fits of this equation to observational data.

### 3.6 The Crab pulsar, PSR B0531+21

We have taken the phase-averaged spectra of the pulsed emission that is received from the Crab pulsar in various frequency bands (the data points shown in Fig. 8) from Lyne & Graham-Smith (2006). The curve in Fig. 8 represents the radiation flux given by equation (4) for the following values of the parameters:

$$\frac{\Omega}{\omega} \simeq 1.9 \times 10^4 \quad \text{with} \quad \frac{\omega}{2\pi} = 30.3 \text{ Hz}, \quad (7)$$

$$S_1 \propto \begin{cases} n^{-11/6} & 3.2 \times 10^6 < n < 10^{12} \\ n^{-1/12} & 10^{12} < n < 7.9 \times 10^{16} \\ n^{-7/12} & 7.9 \times 10^{16} < n < 3.2 \times 10^{22}, \end{cases} \quad (8)$$

$$\frac{S_2}{S_1} \ll 1, \quad \frac{S_3}{S_1} \ll 1 \quad (9)$$

for all  $n$ , and  $m = 10^{12}$ .

Given that the Crab pulsar is at the distance  $R_P \simeq 6.2 \times 10^{21}$  cm (Taylor et al. 1993) and has a light cylinder with



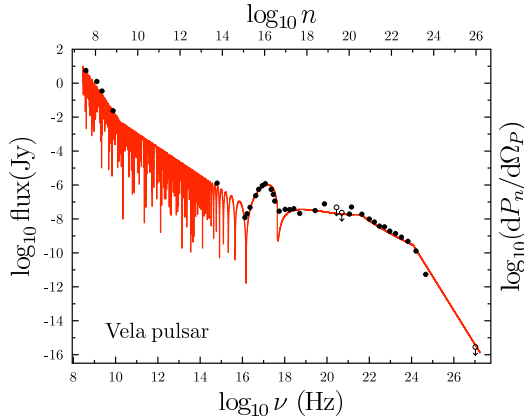


**Figure 9.** The points show observational data (where available) from the spectrum of the Vela pulsar. The curves show the spectral distribution  $\log(dP_n/d\Omega_P)$ , predicted by equations (4), (11) and (12), versus  $\log n$  and  $\log \nu$  for  $\nu = n\omega/(2\pi) \simeq 11.2n$  Hz and  $\Omega/\omega \simeq 2.8 \times 10^5$ . In the model, the recovery of intensity in the X-ray band is caused by resonant enhancement due to the azimuthal modulation frequency  $m\omega/(2\pi) \simeq 1.5 \times 10^{16}$  Hz. The steepening of the gradient of the spectrum by  $-1$  at  $3.6 \times 10^{21}$  Hz reflects the transition through the Rayleigh distance.

the radius  $c/\omega = 1.6 \times 10^8$  cm, the transition through the Rayleigh distance would account for the observed steepening of its spectrum at  $n = 7.9 \times 10^{16}$  (Fig. 8) if the radial extent  $\hat{r}_> - \hat{r}_<$  of the emitting plasma is a fraction  $3.9 \times 10^{-2}$  of the light-cylinder radius.

### 3.7 The Vela pulsar, PSR B0833-45

We have taken the data points shown in Fig. 9 from Thompson et al. (1999) [see also Lyne & Graham-Smith (2006)]. The curve in Fig. 9 represents the radiation flux given by equation (4) for the following values of the parameters:

$$\frac{\Omega}{\omega} \simeq 2.82 \times 10^5 \quad \text{with} \quad \frac{\omega}{2\pi} = 11.2 \text{ Hz}, \quad (10)$$

$$S_1 \propto \begin{cases} n^{-1/2} & 2.5 \times 10^7 < n < 1.3 \times 10^9 \\ n^0 & 1.3 \times 10^9 < n < 1.3 \times 10^{15} \\ n^{3/2} & 1.3 \times 10^{15} < n < 4 \times 10^{16} \\ n^{1/5} & 4 \times 10^{16} < n < 3.2 \times 10^{20} \\ n^{-3/10} & 3.2 \times 10^{20} < n < 10^{23} \\ n^{-1} & 10^{23} < n < 1.6 \times 10^{26}, \end{cases} \quad (11)$$

$$\frac{S_2}{S_1} = 10^7, \quad \frac{S_3}{S_1} \ll 1 \quad (12)$$

for all  $n$ , and  $m = 1.3 \times 10^{15}$ .

Given that the Vela pulsar is at the distance  $R_P \simeq 1.5 \times 10^{21}$  cm (Taylor et al. 1993) and has a light cylinder with the radius  $c/\omega = 4.3 \times 10^8$  cm, the transition through the Rayleigh distance would account for the observed steepening of its spectrum at  $n = 3.2 \times 10^{20}$  (Fig. 9) if the radial extent  $\hat{r}_> - \hat{r}_<$  of the emitting plasma is a fraction  $1.9 \times 10^{-4}$  of the light-cylinder radius.

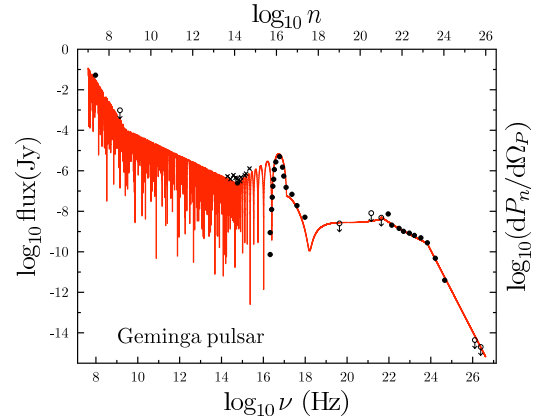


**Figure 10.** The points show observational data (where available) from the spectrum of the Geminga pulsar. The curves show the spectral distribution  $\log(dP_n/d\Omega_P)$ , predicted by equations (4), (14) and (15), versus  $\log n$  and  $\log \nu$  for  $\nu = n\omega/(2\pi) \simeq 4.22n$  Hz and  $\Omega/\omega \simeq 5.89 \times 10^5$ . In the model, the recovery of intensity over the optical and X-ray bands is caused by resonant enhancement due to the azimuthal modulation frequency  $m\omega/(2\pi) \simeq 6.7 \times 10^{14}$  Hz. The steepening of the gradient of the spectrum by  $-1$  at  $4.2 \times 10^{21}$  Hz reflects the crossing of the Rayleigh distance.

### 3.8 The Geminga pulsar, PSR J0633+1746

We have taken the data points shown in Fig. 10 from Thompson et al. (1999) and Kargaltsev et al. (2005) [see also Lyne & Graham-Smith (2006)]. The curve in Fig. 10 represents the radiation flux given by equation (4) for the following values of the parameters:

$$\frac{\Omega}{\omega} \simeq 5.89 \times 10^5 \quad \text{with} \quad \frac{\omega}{2\pi} = 4.22 \text{ Hz}, \quad (13)$$

$$S_1 \propto \begin{cases} n^{-5/12} & 10^7 < n < 1.58 \times 10^9 \\ n^{1/6} & 1.6 \times 10^9 < n < 1.6 \times 10^{14} \\ n^{4/15} & 1.6 \times 10^{14} < n < 3 \times 10^{16} \\ n^{1/4} & 3 \times 10^{16} < n < 10^{21} \\ n^{-1/4} & 10^{21} < n < 1.8 \times 10^{23} \\ n^{-1} & 1.8 \times 10^{23} < n < 10^{26}, \end{cases} \quad (14)$$

$$\frac{S_2}{S_1} = \begin{cases} 0 & 1.6 \times 10^{14} < n < 3 \times 10^{16} \\ 10^7 & \text{otherwise,} \end{cases} \quad (15)$$

$S_3 \ll S_1$  for all  $n$ , and  $m = 1.6 \times 10^{14}$ .

Given that the Geminga pulsar is at the distance  $R_P \simeq 4.6 \times 10^{20}$  cm (Taylor et al. 1993) and has a light cylinder with the radius  $c/\omega = 1.1 \times 10^9$  cm, crossing the Rayleigh distance would account for the observed steepening of its spectrum at  $n = 10^{21}$  (Fig. 10) if the radial extent  $\hat{r}_> - \hat{r}_<$  of the emitting plasma is a fraction  $3.6 \times 10^{-5}$  of the light-cylinder radius.

### 3.9 PSR B0656+14

We have taken the data points shown in Fig. 11 from Shibanov et al. (2006), De Luca et al. (2005), and Karagaltsev et al. (2007). The curve in Fig. 11 represents the

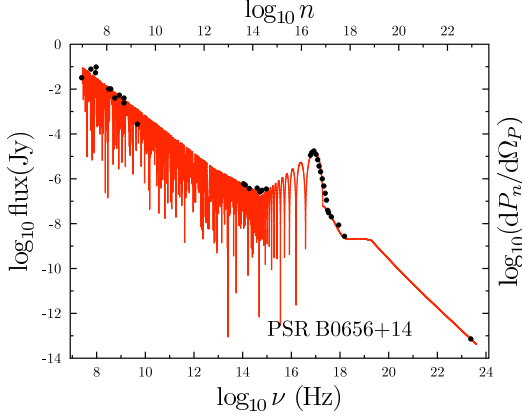


**Figure 11.** The points show observational data (where available) from the spectrum of B0656+14. The curves show the spectral distribution  $\log(dP_n/d\Omega_P)$ , predicted by equations (4), (17) and (18), versus  $\log n$  and  $\log \nu$  for  $\nu = n\omega/(2\pi) \simeq 2.6n$  Hz and  $\Omega/\omega \simeq 5.89 \times 10^5$ . In the model, the recovery of intensity over the optical and X-ray bands is caused by resonant enhancement due to the azimuthal modulation frequency  $m\omega/(2\pi) \simeq 5.2 \times 10^{14}$  Hz. The steepening of the gradient of the spectrum by  $-1$  at  $1.8 \times 10^{19}$  Hz corresponds to crossing the Rayleigh distance.

radiation flux given by equation (4) for the following values of the parameters:

$$\frac{\Omega}{\omega} \simeq 7.94 \times 10^5 \quad \text{with} \quad \frac{\omega}{2\pi} = 2.6 \text{ Hz}, \quad (16)$$

$$S_1 \propto \begin{cases} n^{-1/2} & 10^7 < n < 3.2 \times 10^{12} \\ n^{-3/8} & 3.2 \times 10^{12} < n < 2 \times 10^{14} \\ n^{3/8} & 2 \times 10^{14} < n < 7.6 \times 10^{16} \\ n^0 & 7.6 \times 10^{16} < n < 7.1 \times 10^{18} \\ n^{-1/2} & 7.1 \times 10^{18} < n < 1.58 \times 10^{23}, \end{cases} \quad (17)$$

$$\frac{S_2}{S_1} = \begin{cases} 0 & 10^7 < n < 7.6 \times 10^{16} \\ 1.78 \times 10^6 & \text{otherwise,} \end{cases} \quad (18)$$

$S_3 \ll S_1$  for all  $n$ , and  $m = 2 \times 10^{14}$ .

Given that PSR B0656+14 is at the distance  $R_P \simeq 2.3 \times 10^{21}$  cm (Taylor et al. 1993) and has a light cylinder with the radius  $c/\omega = 1.8 \times 10^9$  cm, the transition through the Rayleigh distance would account for the observed steepening of its spectrum at  $n = 7.1 \times 10^{18}$  (Fig. 11) if the radial extent  $\hat{r}_> - \hat{r}_<$  of the emitting plasma is a fraction  $7.5 \times 10^{-4}$  of the light-cylinder radius.

### 3.10 PSR B1055-52

We have taken the data points shown in Fig. 12 from Thompson et al. (1999) and McCulloch & Hamilton (1976) [see also Lyne & Graham-Smith (2006)]. The curve in Fig. 12 represents the radiation flux given by equation (4) for the following values of the parameters:

$$\frac{\Omega}{\omega} \simeq 6.31 \times 10^5 \quad \text{with} \quad \frac{\omega}{2\pi} = 5.07 \text{ Hz}, \quad (19)$$

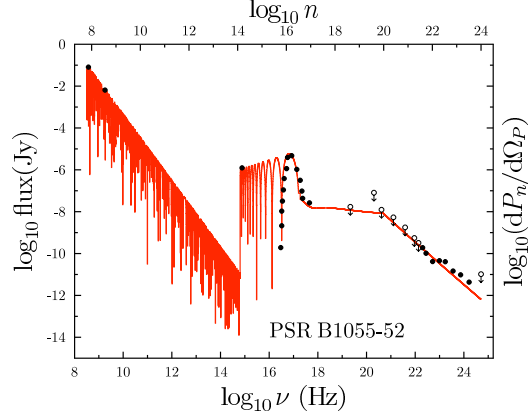


**Figure 12.** The points show observational data (where available) from the spectrum of B1055-52. The curves show the spectral distribution  $\log(dP_n/d\Omega_P)$ , predicted by equations (4), (20) and (21), versus  $\log n$  and  $\log \nu$  for  $\nu = n\omega/(2\pi) \simeq 5.07n$  Hz and  $\Omega/\omega \simeq 6.31 \times 10^5$ . In the model, the recovery of intensity in the optical band is caused by resonant enhancement due to the azimuthal modulation frequency  $m\omega/(2\pi) \simeq 6.6 \times 10^{14}$  Hz. The steepening of the gradient of the spectrum by  $-1$  at  $4.5 \times 10^{20}$  Hz is due to the crossing of the Rayleigh distance.

$$S_1 \propto \begin{cases} n^{-3/8} & 6.3 \times 10^7 < n < 1.3 \times 10^{14} \\ n^{1/10} & 1.3 \times 10^{14} < n < 3.7 \times 10^{16} \\ n^0 & 3.7 \times 10^{16} < n < 8.9 \times 10^{19} \\ n^{-1/2} & 8.9 \times 10^{19} < n < 10^{24}, \end{cases} \quad (20)$$

$$\frac{S_2}{S_1} = \begin{cases} 0 & 1.3 \times 10^{14} < n < 3.7 \times 10^{16} \\ 4.22 \times 10^5 & \text{otherwise,} \end{cases} \quad (21)$$

$S_3 \ll S_1$  for all  $n$ , and  $m = 1.3 \times 10^{14}$ .

Given that PSR B1055-52 is at the distance  $R_P \simeq 4.7 \times 10^{21}$  cm (Taylor et al. 1993) and has a light cylinder with the radius  $c/\omega = 9.4 \times 10^8$  cm, the transition through the Rayleigh distance would account for the observed steepening of its spectrum at  $n = 8.9 \times 10^{19}$  (Fig. 12) if the radial extent  $\hat{r}_> - \hat{r}_<$  of the emitting plasma is a fraction  $4.2 \times 10^{-4}$  of the light-cylinder radius.

### 3.11 PSR B1509-58

We have taken the data points shown in Fig. 13 from Thompson et al. (1999) [see also Lyne & Graham-Smith (2006)]. The curve in Fig. 13 represents the radiation flux given by equation (4) for the following values of the parameters:

$$\frac{\Omega}{\omega} \simeq 5.62 \times 10^5 \quad \text{with} \quad \frac{\omega}{2\pi} = 6.6 \text{ Hz}, \quad (22)$$

$$S_1 \propto \begin{cases} n^{-1/4} & 5 \times 10^7 < n < 2.5 \times 10^{15} \\ n^{-1/6} & 2.5 \times 10^{15} < n < 5 \times 10^{18} \\ n^{-2/3} & 5 \times 10^{18} < n < 1.6 \times 10^{26}, \end{cases} \quad (23)$$

$$\frac{S_2}{S_1} \ll 1, \quad \frac{S_3}{S_1} \ll 1 \quad (24)$$

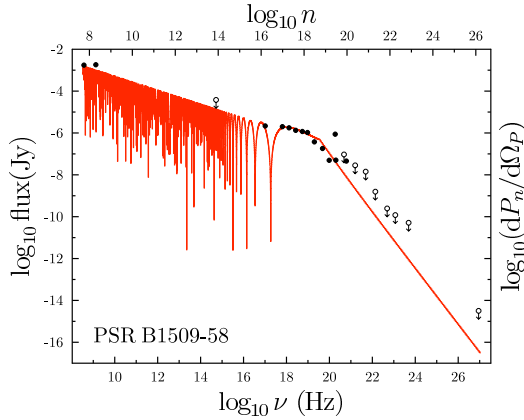


**Figure 13.** The points show observational data (where available) from the spectrum of B1509-58. The curves show the spectral distribution  $\log(dP_n/d\Omega_P)$ , predicted by equations (4), (23) and (24), versus  $\log n$  and  $\log \nu$  for  $\nu = n\omega/(2\pi) \simeq 6.6n$  Hz and  $\Omega/\omega \simeq 5.62 \times 10^5$ . The steepening of the gradient of the spectrum by  $-1$  at  $3.3 \times 10^{19}$  Hz is caused by crossing the Rayleigh distance.

for all  $n$ . (The existing data is insufficient to pinpoint the value of  $m$  for this pulsar.)

Given that PSR B1509-58 is at the distance  $R_P \simeq 1.3 \times 10^{22}$  cm (Taylor et al. 1993) and has a light cylinder with the radius  $c/\omega = 7.2 \times 10^8$  cm, the transition through the Rayleigh distance would account for the observed steepening of its spectrum at  $n = 5 \times 10^{18}$  (Fig. 13) if the radial extent  $\hat{r}_> - \hat{r}_<$  of the emitting plasma is a fraction  $3.4 \times 10^{-3}$  of the light-cylinder radius.

### 3.12 PSR B1706-44

We have taken the data points shown in Fig. 14 from Thompson et al. (1999) [see also Lyne & Graham-Smith (2006)]. The curve in Fig. 14 represents the radiation flux given by equation (4) for the following values of the parameters:

$$\frac{\Omega}{\omega} \simeq 3.71 \times 10^5 \quad \text{with} \quad \frac{\omega}{2\pi} = 9.76 \text{ Hz}, \quad (25)$$

$$S_1 \propto \begin{cases} n^{-1/2} & 3.2 \times 10^7 < n < 3.2 \times 10^{14} \\ n^{1/2} & 3.2 \times 10^{14} < n < 8.3 \times 10^{15} \\ n^{-1/10} & 8.3 \times 10^{15} < n < 2 \times 10^{22} \\ n^{-3/5} & 2 \times 10^{22} < n < 10^{27}, \end{cases} \quad (26)$$

$$\frac{S_2}{S_1} \ll 1, \quad \frac{S_3}{S_1} \ll 1 \quad (27)$$

for all  $n$ , and  $m = 3.2 \times 10^{14}$ .

Given that PSR B1706-44 is at the distance  $R_P \simeq 5.6 \times 10^{21}$  cm (Taylor et al. 1993) and has a light cylinder with the radius  $c/\omega = 4.9 \times 10^8$  cm, the transition through the Rayleigh distance would account for the observed steepening of its spectrum at  $n = 2 \times 10^{22}$  (Fig. 14) if the radial extent  $\hat{r}_> - \hat{r}_<$  of the emitting plasma is a fraction  $4.2 \times 10^{-5}$  of the light-cylinder radius.

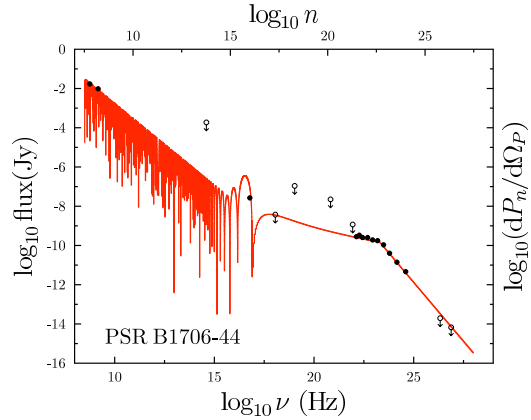


**Figure 14.** The points show observational data (where available) from the spectrum of B1706-44. The curves show the spectral distribution  $\log(dP_n/d\Omega_P)$ , predicted by equations (4), (26) and (27), versus  $\log n$  and  $\log \nu$  for  $\nu = n\omega/(2\pi) \simeq 9.76n$  Hz and  $\Omega/\omega \simeq 3.71 \times 10^5$ . In the model, the recovery of intensity in the optical band is caused by resonant enhancement due to the azimuthal modulation frequency  $m\omega/(2\pi) \simeq 3.1 \times 10^{15}$  Hz. The transit through the Rayleigh distance accounts for the steepening of the gradient of the spectrum by  $-1$  at  $1.9 \times 10^{23}$  Hz.

### 3.13 PSR B1929+10

We have taken the data points shown in Fig. 15 from Becker et al. (2006). The curve in Fig. 15 represents the radiation flux given by equation (4) for the following values of the parameters:

$$\frac{\Omega}{\omega} \simeq 6.3 \times 10^5 \quad \text{with} \quad \frac{\omega}{2\pi} = 4.41 \text{ Hz}, \quad (28)$$

$$S_1 \propto n^{-1/2}, \quad \frac{S_2}{S_1} = 3.16 \times 10^6, \quad 2 \times 10^7 < n < 1.6 \times 10^{14}, \quad (29)$$

$$S_2 \propto n^{3/8}, \quad \frac{S_1}{S_2} \ll 1, \quad 1.6 \times 10^{14} < n < 2.8 \times 10^{17} \quad (30)$$

$S_3$  is negligible for all  $n$ , and  $m = 1.6 \times 10^{14}$ .

Given that PSR B1929+10 is at the distance  $R_P \simeq 5.2 \times 10^{20}$  cm (Taylor et al. 1993) and has a light cylinder with the radius  $c/\omega = 1.1 \times 10^9$  cm, the absence of a sudden steepening in the gradient of its spectrum (Fig. 15) means that the transition through the Rayleigh distance must occur at harmonic numbers larger than  $n = 2.8 \times 10^{17}$ , and so the radial extent  $\hat{r}_> - \hat{r}_<$  of the emitting plasma must be smaller than a fraction  $2.3 \times 10^{-3}$  of the light-cylinder radius.

### 3.14 PSR B1951+32

We have taken the data points shown in Fig. 16 from Thompson et al. (1999) [see also Lyne & Graham-Smith (2006)]. The curve in Fig. 16 represents the radiation flux given by equation (4) for the following values of the parameters:

$$\frac{\Omega}{\omega} \simeq 1.41 \times 10^5 \quad \text{with} \quad \frac{\omega}{2\pi} = 25.3 \text{ Hz}, \quad (31)$$

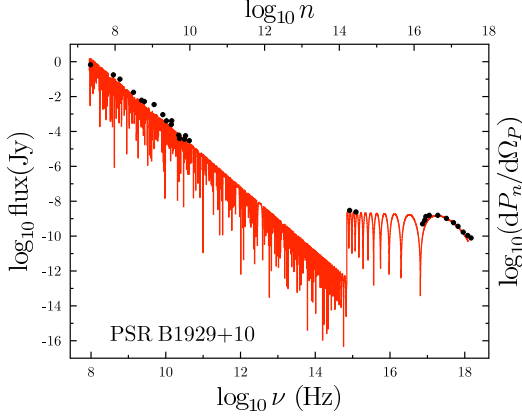


**Figure 15.** The points show observational data (where available) from the spectrum of B1929+10. The curves show spectral distribution  $\log(dP_n/d\Omega_P)$ , predicted by equations (4), (29) and (30), versus  $\log n$  and  $\log \nu$  for  $\nu = n\omega/(2\pi) \simeq 4.41n$  Hz and  $\Omega/\omega \simeq 6.3 \times 10^5$ . In the model, the recovery of intensity in the optical band is caused by resonant enhancement due to the azimuthal modulation frequency  $m\omega/(2\pi) \simeq 7 \times 10^{14}$  Hz.

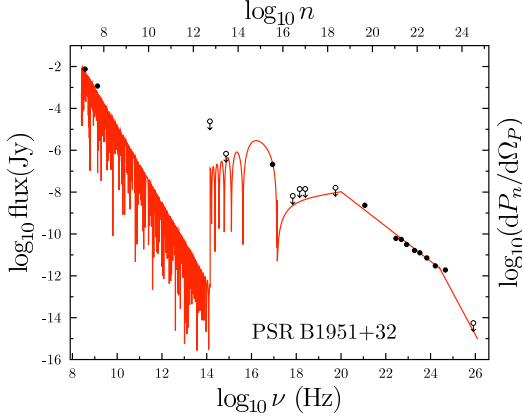


**Figure 16.** The points show observational data (where available) from the spectrum of B1951+32. The curves show the spectral distribution  $\log(dP_n/d\Omega_P)$ , predicted by equations (4), (32) and (33), versus  $\log n$  and  $\log \nu$  for  $\nu = n\omega/(2\pi) \simeq 25.3n$  Hz and  $\Omega/\omega \simeq 1.41 \times 10^5$ . In the model, the recovery of intensity in the optical band is caused by resonant enhancement due to the azimuthal modulation frequency  $m\omega/(2\pi) \simeq 1.4 \times 10^{14}$  Hz. The crossing of the Rayleigh distance accounts for the steepening of the gradient of the spectrum by  $-1$  at  $10^{20}$  Hz.

$$S_2 \propto \begin{cases} n^{-1/2} & 10^7 & < n < & 5.6 \times 10^{12} \\ n^{3/4} & 5.6 \times 10^{12} & < n < & 5.6 \times 10^{15} \\ n^{5/12} & 5.6 \times 10^{15} & < n < & 4 \times 10^{18} \\ n^{-1/12} & 4 \times 10^{18} & < n < & 10^{23} \\ n^{-2/3} & 10^{23} & < n < & 5 \times 10^{24}, \end{cases} \quad (32)$$

$$\frac{S_1}{S_2} \ll 1, \quad \frac{S_3}{S_2} \ll 1 \quad (33)$$

for all  $n$ , and  $m = 5.6 \times 10^{12}$ .

**Table 3.** Summary of  $\Omega$  values used in fitting pulsar spectra. The parameter  $f_p$  is the derived plasma frequency, where we assume that  $f_p \equiv \Omega/2\pi$ .  $N_e$  is the electron density in the emitting region of the pulsar's atmosphere calculated from the plasma frequency  $f_p$ , using  $(2\pi f_p)^2 = 4\pi N_e e^2/m_e$ , where  $e$  is the electron's charge and  $m_e$  is its mass.

Pulsar	$\frac{\Omega}{\omega}$	$\frac{\omega}{2\pi}$ (Hz)	$f_p$ (MHz)	$N_e$ ( $10^4 \text{cm}^{-3}$ )
PSR B0531+21	19000	30.3	0.58	0.4
PSR B0833-45	282000	11.2	3.2	12
PSR J0633+1746	589000	4.22	2.5	7.7
PSR B0656+14	794000	2.6	2.1	5.3
PSR B1055-52	631000	5.07	3.2	13
PSR B1509-58	562000	6.6	3.7	17
PSR B1706-44	371000	9.76	3.6	16
PSR B1929+10	630000	4.41	2.8	9.6
PSR B1951+32	141000	25.3	3.6	16

Given that PSR B01951+32 is at the distance  $R_P \simeq 7.7 \times 10^{21}$  cm (Taylor et al. 1993) and has a light cylinder with the radius  $c/\omega = 1.9 \times 10^8$  cm, the transit through the Rayleigh distance would account for the observed steepening of its spectrum at  $n = 4 \times 10^{18}$  (Fig. 16) if the radial extent  $\hat{r}_> - \hat{r}_<$  of the emitting plasma is a fraction  $5.6 \times 10^{-3}$  of the light-cylinder radius.

## 4 DISCUSSION

### 4.1 Fitted values of $\Omega$ and inferred plasma frequencies

The fitted values of  $\Omega/\omega$  taken from Section 3 are summarized in Table 3, where we have also converted the  $\Omega/2\pi$  values into Hz using the known rotation frequencies of the pulsars. It will be remembered that  $\Omega/2\pi$  represents a characteristic frequency that modulates the source [see equation (3)] in the emitting region; assuming that the pulsar magnetosphere consists of a dilute neutral plasma (Spitkovsky 2006), it is reasonable to make the attribution  $\Omega/2\pi = f_p$ , where  $f_p$  is the (electron) plasma frequency in the emitting part of the magnetosphere. The fifth column of Table 3 gives inferred electron densities  $N_e$  derived using  $(2\pi f_p)^2 = 4\pi N_e e^2/m_e$ , where  $e$  is the electron's charge and  $m_e$  is its mass (Lyne & Graham-Smith 2006). Note that virtually all of the electron densities are of the order of  $10^5 \text{cm}^{-3}$ , with only the Crab's value ( $N_e = 4 \times 10^3 \text{cm}^{-3}$ ) being somewhat lower.<sup>1</sup> Nevertheless, all of these  $N_e$  are completely consistent with the densities expected in a conventional pulsar magnetosphere (Lyne & Graham-Smith 2006).

Another way of visualizing the rather similar values of

<sup>1</sup> The lower electron density around the Crab could result from its very high optical luminosity (Lyne & Graham-Smith 2006), which might act to "blow" electrons out of the magnetosphere.

$\Omega$  found in Section 3 for all of the pulsars is to plot  $\Omega/\omega$  versus  $\omega/2\pi$  (Fig. 17); the values of  $\Omega/\omega$  all lie close to the curve  $\Omega/\omega = 2.56 \times 10^6(2\pi/\omega)$ .

Given that positions of the last peaks of the Airy functions appearing in equation (4) and hence the salient features of the pulsar spectrum scale as  $(\Omega/\omega)^3$ , the rather uniform values of  $\Omega$  imply that slower pulsars (those with smaller values of  $\omega$ ) will have observed spectral intensities weighted towards higher frequencies. By contrast, millisecond pulsars (with large  $\omega$ ) should have emission concentrated at lower frequencies than the above pulsars. These predictions seem to be borne out both by the radio-quiet pulsar in the supernova remnant CTA1 ( $\omega/2\pi \simeq 3.1$  Hz), which has emission peaked in the gamma-ray end of the spectrum (Abdo et al. 2008), and by millisecond pulsars such as J1748-22446ad ( $\omega/2\pi \simeq 716$  Hz), B1937+21 ( $\omega/2\pi \simeq 642$  Hz) and B1957+20 ( $\omega/2\pi \simeq 622$  Hz) which show no emission in the high-frequency range but generally strong and bright pulses at radio frequencies (Soglasnov et al. 2004; Hessels et al. 2006; Huang & Becker 2007).

#### 4.2 The frequency $m\omega/2\pi$ and inferred magnetic fields

Table 4 shows the values of  $m$  derived from the frequencies at which the observed spectra recover their intensity as a result of resonance enhancement (see Section 3). The frequency  $m\omega/2\pi$  represents the frequency of azimuthal fluctuations of the polarization-current distribution pattern. These spatial fluctuation frequencies ( $\sim 10^{13} - 10^{15}$  Hz) could well arise from the cyclotron resonance of electrons. The cyclotron (angular) frequency  $\omega_c$  in a field  $H$  is defined as  $\omega_c = eH/cm_e$ , where  $m_e$  is the mass of the electron and  $e$  is its charge (cgs units) (Lyne & Graham-Smith 2006); hence, we can use the  $m\omega$  values to infer magnetic fields of around  $10^7 - 10^9$  G in the emitting region (Table 4). Such fields are completely consistent with those expected in a conventional pulsar magnetosphere (Lyne & Graham-Smith 2006).

#### 4.3 The size of the emitting region

The set of frequencies at which the slopes of the observed spectra suddenly steepen by  $-1$  mostly lie in the range  $10^{18} - 10^{21}$  Hz. This implies that the radial extent of the emitting polarization current is a fraction  $10^{-2} - 10^{-5}$  of the light-cylinder radius (Section 3). Recalling that the subbeam that arises from the emitting part of the source in the radial interval  $\hat{r}_< \leq \hat{r} \leq \hat{r}_>$  (where  $\hat{r} \equiv r\omega/c$ ) is detectable within the polar interval  $\arccos(1/\hat{r}_<) \leq |\theta_P - \pi/2| \leq \arccos(1/\hat{r}_>)$  (see Section 2.3.1), it follows that the polar widths  $\Delta\theta_P \simeq \sin\theta_P \tan\theta_P(\hat{r}_> - \hat{r}_<)$  of the subbeams that are detected outside the plane of rotation ( $\theta_P \neq \pi/2$ ) are of the order of  $10^{-2} - 10^{-5}$  radians. [Note that the overall radiation beam consists of a superposition of such narrow subbeams (Section 2.3.1).]

#### 4.4 Frequency dependence of Fourier components of the source density $\mathbf{s}$

The dependence of the Fourier components  $\bar{s}_{r,\varphi,z}$  of the source densities  $s_{r,\varphi,z}$  on frequency (or on harmonic number

**Table 4.** Summary of  $m$  values used in fitting pulsar spectra. The final column tabulates the magnetic fields deduced on the assumption that  $m\omega/2\pi$  represents the cyclotron resonance of electrons in the emitting region of the magnetosphere. These were derived using the standard equation for the cyclotron (angular) frequency  $\omega_c$ :  $m\omega = \omega_c \equiv eH/cm_e$ , where  $e$  is the electron's charge and  $m_e$  is its mass.

Pulsar	$m$	$\frac{\omega}{2\pi}$ (Hz)	$\frac{m\omega}{2\pi}$ (THz)	$H$ (G)
PSR B0531+21	$10^{12}$	30.3	30	$1.1 \times 10^7$
PSR B0833-45	$1.3 \times 10^{15}$	11.2	15000	$5.2 \times 10^9$
PSR J0633+1746	$1.6 \times 10^{14}$	4.22	680	$2.4 \times 10^8$
PSR B0656+14	$2 \times 10^{14}$	2.6	520	$1.9 \times 10^8$
PSR B1055-52	$1.3 \times 10^{14}$	5.07	660	$2.4 \times 10^8$
PSR B1509-58	–	6.6	–	–
PSR B1706-44	$3.2 \times 10^{14}$	9.76	3100	$1.1 \times 10^9$
PSR B1929+10	$1.6 \times 10^{14}$	4.41	710	$2.5 \times 10^8$
PSR B1951+32	$5.6 \times 10^{12}$	25.3	140	$5.1 \times 10^7$

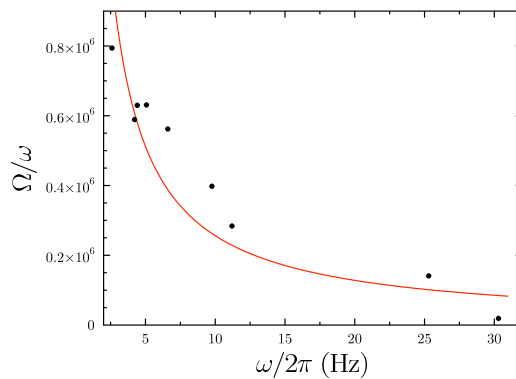


**Figure 17.** The points designate the values of the two parameters  $\Omega/\omega$  and  $\omega/2\pi$  for the 9 pulsars considered in Section 3, and the curve  $\Omega/\omega = 2.56 \times 10^6(2\pi/\omega)$  represents the best fit to these points.

$n$ ) is determined by the fluctuations (within the emitting region) of  $s_{r,\varphi,z}$  with the coordinate  $z$  [see equation (A27)]. The small-scale spatial variations of  $\mathbf{s}$  in the direction parallel to the rotation axis that are implied by the observational data (see Section 3) may be identified with the sharp gradients in the distribution of the source density at a current sheet. The two-dimensional current sheets predicted by numerical models of MHD pulsar magnetospheres extend beyond the light cylinder. Not only do they have distribution patterns that rotate superluminally (Spitkovsky 2006), but they also vary discontinuously, and so have fluctuations that occur over wide ranges of length scales and amplitudes.

## 5 SUMMARY AND CONCLUSION

We have compared the observed spectra of 9 pulsars for which multiwavelength data are available with the spectrum of the radiation generated by an extended source in superluminal rotation and shown that the entire spectrum of each pulsar can be accounted for quantitatively in terms of this single emission process. The results reported here are model-independent in that the only global property of the magnetospheric structure invoked is its quasi-steady time dependence: the cylindrical components  $j_{r,\varphi,z}(r, \varphi, z; t)$  of the density of the magnetospheric polarization current depend on  $\varphi$  only in the combination  $\varphi - \omega t$ . This property follows unambiguously from the observational data and implies that a current distribution with a superluminally rotating pattern at a radius  $r > c/\omega$  is responsible for the unique features of pulsar emission such as the pulses' extreme brightness temperature, temporal width, source dimension and peak spectral frequency as well as the average pulses' polarization properties (their occurrence as concurrent 'orthogonal' modes with swinging position angles and with nearly 100 per cent linear or circular polarization).

The curves in Figs. 8–16 demonstrate that the universal features of pulsar spectra (their breadth over 15–18 orders of magnitude of frequency, the recovery of their amplitudes in the optical band, their bell-shaped peaks in ultraviolet, and the sudden steepening of their gradient by  $-1$  in the X-ray band) are all described by the properties of the Green function for the problem, and so are consequences solely of the accelerated superluminal motion of the distribution pattern of their source. Only the finer details of these spectra depend on the structure of the pulsar magnetosphere, or more specifically, on the structure of the current sheets just outside the light cylinder of the pulsar magnetosphere (Spitkovsky 2006) (i.e. on the variable 'weather' in the pulsar magnetosphere, as opposed to its stable 'climate').

The increase in the spacing between successive peaks of the oscillating spectra shown in Figs. 8–16 with frequency, which has already been observed in the radio emission from the Crab pulsar (Hankins & Eilek 2007), also only depends on the properties of the Airy functions in equation (4); it is another universal feature of the pulsar emission predicted by the present model that can be tested, in principle, over any frequency band [see Fig. 7 and Ardavan et al. (2008a)].

## 6 ACKNOWLEDGMENTS

We are grateful to Quinn Marksteiner for helpful comments. This work is supported by U.S. Department of Energy Grant LDRD 20080085DR, "Construction and use of superluminal emission technology demonstrators with applications in radar, astrophysics and secure communications". A. Ardavan thanks the Royal Society for support.

## REFERENCES

- Abdo A.A. et al., 2008, *Science* 322, 1218  
 Abramowitz M., Stegun I.A., 1970, *Handbook of Mathematical Functions* (Dover)  
 Ardavan H., 1998, *Phys Rev E*, 58, 6659  
 Ardavan H., Ardavan A., Singleton J., 2003, *J Opt Soc Am A*, 20, 2137  
 Ardavan H., Ardavan A., Singleton J., 2004a, *J Opt Soc Am A*, 21, 858  
 Ardavan A., Hayes W., Singleton J., Ardavan H., Fopma J., Halliday D., 2004b, *J Appl Phys*, 96, 7760  
 Ardavan H., Ardavan A., Singleton J., Fasel J., Schmidt, A., 2007, *J Opt Soc Am A*, 24, 2443  
 Ardavan H., Ardavan A., Singleton J., Perez, M.R., 2008a, *MNRAS*, 388, 873  
 Ardavan H., Ardavan A., Singleton J., Fasel J., Schmidt A., 2008b, *J Opt Soc Am A*, 25, 780  
 Bessarab A.V., Gorbunov A.A., Martynenko S.P., Prudkoy N.A., 2004, *IEEE Trans Plasma Sci*, 32, 1400  
 Becker W., Kramer M., Jessner A., Taam R.E., Jia J.J., Cheng K.S., Mignani R., Pellizzoni A., De Luca A., Slowikowska A., Caraveo P.A., 2006, *ApJ*, 645, 1421  
 Bolotovskii B.M., Ginzburg V.L., 1972, *Sov Phys Usp*, 15, 184  
 Bolotovskii B.M., Bykov V.P., 1990, *Sov Phys Usp*, 33, 477  
 Bolotovskii B.M., Serov A.V., 2005, *Phys Usp*, 43, 903  
 Borovikov, V.A., 1994, *Uniform Stationary Phase Method* (Institution of Electrical Engineers)  
 Brooker G., 2003, *Modern Classical Optics*, 1st ed. (Oxford University Press)  
 Caraveo P.A., De Luca A., Mereghetti S., Pellizzoni A., Bignami G.F., 2004, *Science*, 305, 376  
 Cusumano G., Hermsen W., Kramer M., Kuiper L., Löhmer O., Massaro E., Mineo T., Nicastro L., Stappers W., 2003, *A&A*, 410, L9  
 De Luca A., Caraveo P.A., Mereghetti S., Negroni M., Bignami G.F., 2005, *ApJ*, 623, 1051  
 Ginzburg V.L., 1972, *Sov Phys JETP*, 35, 92  
 Hankins T.H., Kern J.S., Weatherall J.C., Eilek J.A., 2003, *Nature*, 422, 141  
 Hankins T.H., Eilek J.A., 2007, *Ap J*, 670, 693  
 Harding A.K., Stern J.V., Dycks J., Frackowiak M., 2008, *ApJ*, 680, 1378  
 Hessels J.W.T., Ransom S.M., Stairs I.H., Freire P.C.C., Kaspi V.M., Camilo F., 2006, *Science*, 311, 1901  
 Huang H.H., Becker W., 2007, *A&A*, 463, L5  
 Jackson J.D., 1999, *Classical Electrodynamics*, 3rd ed. (Wiley)  
 Kargaltsev O.Y., Pavlov G.G., Zavlin V.E., Romani R.W., 2005, *ApJ*, 625, 307  
 Karagaltsev O., Pavlov G., 2007, *Ap&SS*, 308, 287  
 Kuiper L., Hermsen W., Cusumano G., Diehl R., Schönfelder V., Stron A., Bennett K., McConnell M.L., 2001, *A&A*, 378, 918  
 Kuiper L., Hermsen W., Verbunt F., Ord S., Stairs I., Lyne A., 2002, *ApJ*, 577, 917  
 Lommen A., Donovan J., Gwinn C., Arzoumanian Z., Harding A., Strickman M., Dodson R., McCulloch P., Moffett D., 2007, *ApJ*, 657, 436  
 Lyne A.G., Graham-Smith F., 2006, *Pulsar Astronomy* (Cambridge U Press)  
 McCulloch P.M., Hamilton P.A., 1976, *MNRAS*, 175, 71P  
 Moffett D.A., Hankins T.H., 1996, *ApJ*, 468, 779  
 Ruderman M.A., Sutherland P.G., 1975, *ApJ*, 196, 51  
 Schmidt, A., Ardavan H., Fasel J., Singleton J., Ardavan A., 2007, in Becker W., Huang H.H., eds, *MPE Report 291*, Proc. 363rd WE-Heraeus Seminar on Neutron Stars



and Pulsars, p. 124

Slowikowska A., Jessner A., Klein B., and Kanbach G., 2005, *astro-ph/0511599v2*.

Shibanov Y.A., Zharikov S.V., Komarova V.N., Kawai N., Urata Y., Koptsevich A.B., Sokolov V.V., Shibata S., Shibazaki N., 2006, *A&A*, 448, 313

Singleton J., Ardavan A., Ardavan H., Fopma J., Halliday D., Hayes W., 2004, in *Digest of the 2004 Joint 29th International Conference on Infrared and Millimeter Waves and 12th International Conference on Terahertz Electronics* (IEEE), 591

Soglasnov V.A., Popov M.V., Bartel N., Cannon W., Novikov A. Yu., Kondratiev V. I., Altunin, V.I., 2004, *ApJ*, 616,439

Spitkovsky A., 2006, *Ap J*, 648, L51

Taylor J.H., Manchester R.N., Lyne A.G., 1993, *ApJS*, 88, 529

Thompson D.J. et al., 1999, *ApJ*, 516, 297

Zavlin V.E., 2007, *arXiv:astro-ph/0702426*

## APPENDIX A: MATHEMATICAL DESCRIPTION OF THE RADIATED FIELD

A general mathematical treatment of spectrum of the radiation field that is generated by the source distribution described in equation (3) has already been given in Ardavan et al. (2003). Our purpose in this appendix is to make the physical content of the previous analysis more transparent by presenting its results from an alternative point of view. We begin by calculating the spectrum of the radiation emitted by one of the constituent rings of source (3): by first deriving the spectrum of the Liénard-Wiechert potential due to a superluminally rotating point source, and then superposing the potentials of the point-like line elements that make up the ring. Once we have clarified the origin of the higher frequencies in the emission from this simpler ring current, we will further superpose the fields of the rings that make up the volume-distributed source (3) to arrive at the spectrum on which the modelling of the observed spectra considered in this paper is based.

### A1 Radiation field of a constituent ring of the source

The trajectory of a uniformly rotating point source, e.g. the source of synchrotron radiation, is described by

$$r = r_0, \quad z = z_0, \quad \varphi = \varphi_0 + \omega t, \quad (\text{A1})$$

where the subscript 0 denotes the constant values of the cylindrical polar coordinates  $(r, \varphi, z)$  of the point source at time  $t = 0$ , and  $\omega$  is constant. (Note that, to describe repeated rotations,  $\varphi$  in this equation increases indefinitely as the time  $t$  does.) If this source has a strength  $s$  that oscillates with the frequency  $\Omega$  in time, then the density of the polarization current it carries can be written as

$$\mathbf{j} = s\omega \exp(i\Omega t) \delta(r - r_0) \delta(z - z_0) \delta(\varphi - \varphi_0 - \omega t) \hat{\mathbf{e}}_\varphi, \quad (\text{A2})$$

where  $\delta$  is the Dirac delta function, and  $\hat{\mathbf{e}}_\varphi$  is the base vector associated with the azimuthal coordinate  $\varphi$ .

The vector potential due to this oscillating, rotating point source is given by

$$\begin{aligned} \mathbf{A}^{\text{point}} &= \frac{1}{c} \int r dr d\varphi dz dt \mathbf{j} \frac{\delta(t_P - t - R/c)}{R} \\ &= \frac{sr_0\omega}{c} \int dt \exp(i\Omega t) \frac{\delta(t_P - t - R_0/c)}{R_0} \hat{\mathbf{e}}_{\varphi_0}, \quad (\text{A3}) \end{aligned}$$

in which

$$R_0 = R|_{r=r_0, \varphi=\varphi_0+\omega t, z=z_0}, \quad \hat{\mathbf{e}}_{\varphi_0} = \hat{\mathbf{e}}_\varphi|_{r=r_0, \varphi=\varphi_0+\omega t, z=z_0}, \quad (\text{A4})$$

with

$$R = [(z_P - z)^2 + r_P^2 + r^2 - 2rr_P \cos(\varphi_P - \varphi)]^{1/2}, \quad (\text{A5})$$

and

$$\hat{\mathbf{e}}_\varphi = \sin(\varphi_P - \varphi) \hat{\mathbf{e}}_{r_P} + \cos(\varphi_P - \varphi) \hat{\mathbf{e}}_{\varphi_P}, \quad (\text{A6})$$

where  $(\hat{\mathbf{e}}_{r_P}, \hat{\mathbf{e}}_{\varphi_P}, \hat{\mathbf{e}}_{z_P})$  are the constant base vectors associated with the coordinates  $(r_P, \varphi_P, z_P)$  at the observation point  $P$ , and  $c$  is the speed of light *in vacuo*. Evaluation of the remaining integral with respect to  $t$  yields

$$\begin{aligned} \mathbf{A}^{\text{point}} &= \frac{sr_0\omega}{c} \sum_{t=t_j} \frac{\exp(i\Omega t)}{|R_0 - (r_0 r_P \omega / c) \sin(\varphi_P - \varphi_0 - \omega t)|} \\ &\quad \times [\sin(\varphi_P - \varphi_0 - \omega t) \hat{\mathbf{e}}_{r_P} \\ &\quad + \cos(\varphi_P - \varphi_0 - \omega t) \hat{\mathbf{e}}_{\varphi_P}], \quad (\text{A7}) \end{aligned}$$

where the retarded times  $t_j$  are the solutions of

$$t_P = t + R_0/c \quad (\text{A8})$$

[see, e.g. Jackson (1999)]. Depending on the values of  $(r_0, \varphi_0, z_0)$ , there are either one or three  $t_j$ s when the speed  $r_0\omega$  of the source exceeds  $c$  moderately [see Fig. 1, and Ardavan (1998)].

Taking the curl of  $\mathbf{A}^{\text{point}}$ , and noting that the dependence of this potential on the coordinates of a far-field observer arises primarily from the dependence of the retarded times  $t_j$  on these coordinates, we obtain the following expression for the magnetic field of the radiation emitted by the above point source:

$$\begin{aligned} \mathbf{B}^{\text{point}} &= -\frac{sr_0\omega^2}{c^3} \sum_{t=t_j} \frac{1}{|1 - \hat{r}_0 \hat{r}_P \sin(\varphi_P - \varphi_0 - \omega t) / \hat{R}_0|} \\ &\quad \times \frac{d}{dt} \left[ \frac{\exp(i\Omega t) \mathbf{p}}{\hat{R}_0 - \hat{r}_0 \hat{r}_P \sin(\varphi_P - \varphi_0 - \omega t)} \right], \quad (\text{A9}) \end{aligned}$$

with

$$\mathbf{p} = \cos \theta_P \sin(\varphi_P - \varphi_0 - \omega t) \hat{\mathbf{e}}_{\parallel} + \cos(\varphi_P - \varphi_0 - \omega t) \hat{\mathbf{e}}_{\perp}, \quad (\text{A10})$$

where  $\hat{\mathbf{e}}_{\parallel} = \hat{\mathbf{e}}_{\varphi_P}$  (which is parallel to the plane of rotation) and  $\hat{\mathbf{e}}_{\perp} = \hat{\mathbf{n}} \times \hat{\mathbf{e}}_{\parallel}$  comprise a pair of unit vectors normal to the radiation direction

$$\hat{\mathbf{n}} = \sin \theta_P \hat{\mathbf{e}}_{r_P} + \cos \theta_P \hat{\mathbf{e}}_{z_P}, \quad (\text{A11})$$

and  $\hat{r}_0 = r_0\omega/c$ ,  $\hat{r}_P = r_P\omega/c$ , and  $\hat{R}_0 = R_0\omega/c$ . This is the familiar Liénard-Wiechert field, except that it receives contributions from more than one retarded time  $t_j$  if  $\hat{r}_0 > 1$  and so the source moves faster than light (see Section 2).

Next, let us consider a rotating ring  $r = r_0$ ,  $z = z_0$ , whose strength varies spatially, as  $\cos(m\varphi_0)$ , in addition to oscillating temporally ( $m$  is an integer). The field due to such a ring can be obtained from the field  $\mathbf{B}^{\text{point}}$  of the

above point source by multiplying  $\mathbf{B}^{\text{point}}$  by  $\cos(m\varphi_0)$  and superposing the contributions of the elements that make up the ring: elements whose azimuthal positions  $\varphi_0$  at  $t = 0$  cover a full circle only once, and so are labelled uniquely by their initial coordinates over the interval  $-\pi < \varphi_0 \leq \pi$ . That is to say,

$$\mathbf{B}^{\text{ring}} = \int_{-\pi}^{\pi} \mathbf{B}^{\text{point}} \cos(m\varphi_0) d\varphi_0, \quad (\text{A12})$$

with a range of integration that is limited to  $2\pi$ . [Note that the variable  $\varphi_0$  is the same as the variable  $\hat{\varphi}$  appearing in equation (3).]

For  $\hat{r}_0 < 1$ , the denominators in equation (A9) nowhere vanish, and so  $\mathbf{B}^{\text{point}}$  is a regular and periodic function of  $\varphi_0 + \omega t_P$ : according to equation (A8),  $t_j - t_P$  are periodic functions of  $\varphi_0 + \omega t_P$  with the period  $2\pi/\omega$ . In this subluminal case, the expression on the right-hand side of equation (A12) constitutes the coefficient of a single term in the cosine series for  $\mathbf{B}^{\text{point}}$ . Thus the Fourier expansion of  $\mathbf{B}^{\text{ring}}$  consists of only two sinusoidal functions of  $\varphi_0 + \omega t_P$  with the frequencies  $\Omega \pm m\omega$ . For  $\hat{r}_0 > 1$ , on the other hand, the denominators in equation (A9) vanish for a source point  $(r_0, \varphi_0, z_0)$  that approaches the observer with the speed of light and zero acceleration at the retarded time: the expression appearing in the first denominator in this equation equals  $1 + c^{-1}dR_0/dt$ . Being non-integrable (Ardavan et al. 2004a), this singularity makes it impossible to Fourier analyze the representation (A9) of the Liénard-Wiechert field  $\mathbf{B}^{\text{point}}$  directly to obtain the spectral distribution of this field.

The way to handle the singularity of  $\mathbf{B}^{\text{point}}$  in the superluminal case is to go back one step and instead expand the integrand in equation (A3) in a Fourier series with respect to  $\varphi_0$ . (We must use a Fourier series, rather than a Fourier integral, because the values of  $\varphi_0$  over which this function is defined lie in an interval of finite length.) The result is

$$\mathbf{A}^{\text{point}} = \frac{sr_0\omega^2}{2\pi c} \sum_{n=-\infty}^{\infty} \exp(in\omega t_P) \int dt R_0^{-1} \times \exp\{-i[n\omega(t + R_0/c) - \Omega t]\} \hat{\mathbf{e}}_{\varphi_0}, \quad (\text{A13})$$

as can be readily seen by replacing the delta function in equation (A3) by its Fourier-series representation. Taking the curl of this, we then obtain

$$\mathbf{B}^{\text{point}} = \frac{sr_0\omega^3}{2\pi ic^2} \sum_{n=-\infty}^{\infty} n \exp(in\omega t_P) \int dt R_0^{-1} \times \exp\{-i[n\omega(t + R_0/c) - \Omega t]\} \times [\cos\theta_P \sin(\varphi_P - \varphi_0 - \omega t) \hat{\mathbf{e}}_{\parallel} + \cos(\varphi_P - \varphi_0 - \omega t) \hat{\mathbf{e}}_{\perp}]. \quad (\text{A14})$$

For a radiation frequency  $n\omega/2\pi$  that appreciably exceeds the rotation frequency, the asymptotic value of the integral in the above expression receives contributions solely from the stationary points of the phase,  $ct + R_0(t)$ , of the rapidly oscillating exponential in its integrand.

This phase is stationary, in the course of each rotation, at the following two retarded times at which the source approaches the observer along the radiation direction with the speed  $c$ :

$$\omega t_{\pm} = \varphi_P - \varphi_0 + \frac{3\pi}{2} \pm \arccos\left(\frac{1}{\hat{r}_0 \sin\theta_P}\right) + 2k\pi, \quad (\text{A15})$$

where  $(R_P, \theta_P, \varphi_P)$  (with  $R_P \gg c/\omega$ ) denote the spherical polar coordinates of the observation point and  $k$  is an integer. These stationary points coalesce if the observer is located at  $\theta_P = \arcsin(1/\hat{r}_0)$ , i.e. when the source approaches the observer not only with the speed  $c$  but also with zero acceleration [see Fig. 1, and Ardavan et al. (2007)]. In this case, the rapid oscillations of the exponential in equation (A14) result in the destructive interference of contributions from all emission times, except those made during a short interval centred at  $t = t_c$ , where  $\omega t_c = \varphi_P - \varphi_0 + 3\pi/2 + 2k\pi$ .

For  $n \gg 1$  and  $\theta_P = \arcsin(1/\hat{r}_0)$ , we can therefore obtain the leading term in the asymptotic expansion of the integral in equation (A14) by applying the principle of stationary phase: by approximating both the phase  $ct + R_0(t)$  and the amplitude of the rapidly oscillating exponential with the dominant terms in their Taylor expansions about  $t = t_c$  and replacing the limits of integration with  $\pm\infty$  (Borovikov 1994). Evaluation of the resulting integral with the aid of equation (10.4.32) of Abramowitz & Stegun (1970) thus yields

$$\mathbf{B}^{\text{point}} \simeq \frac{2sr_0\omega^2}{ic^2 R_P} \sum_{|n| \gg 1} \left(\frac{n}{2}\right)^{2/3} \exp\{i[n(\omega t_P - \hat{R}_P + \hat{z}_0 \cos\theta_P) + (n - \Omega/\omega)(\varphi_0 - \varphi_P - 3\pi/2)]\} \times \left\{ \cos\theta_P \text{Ai}\left[-\left(\frac{2}{n}\right)^{1/3} \frac{\Omega}{\omega}\right] \hat{\mathbf{e}}_{\parallel} + i\left(\frac{2}{n}\right)^{1/3} \text{Ai}'\left[-\left(\frac{2}{n}\right)^{1/3} \frac{\Omega}{\omega}\right] \hat{\mathbf{e}}_{\perp} \right\}, \quad (\text{A16})$$

where Ai and Ai' stand for the Airy function and the derivative of the Airy function with respect to its argument, respectively, and  $\hat{R}_P = R_P\omega/c$  and  $\hat{z}_0 = z_0\omega/c$ .

Amplitudes of the individual terms in equation (A16) have the dependence  $n^{-1/4}$  on  $n$  for  $n \gg 1$ , so that this series yields a divergent value for  $\mathbf{B}^{\text{point}}$  on the cusp locus  $\theta_P = \arcsin(1/\hat{r}_0)$ , as did equation (A14). However, these individual Fourier components are not periodic functions of  $\varphi_0$  when  $\Omega$  differs from an integral multiple of  $\omega$ . As a result, when we insert equation (A16) in equation (A12) and carry out the integration with respect to  $\varphi_0$ , we obtain an expression that contains all values of  $(n \gg 1)$ :

$$\mathbf{B}^{\text{ring}} \simeq \frac{2sr_0\omega^2}{ic^2 R_P} \sum_{|n| \gg 1} \left(\frac{n}{2}\right)^{2/3} C_{\varphi_0} \exp\{i[n(\omega t_P - \hat{R}_P + \hat{z}_0 \cos\theta_P) - (n - \Omega/\omega)(\varphi_P + 3\pi/2)]\} \times \left\{ \cos\theta_P \text{Ai}\left[-\left(\frac{2}{n}\right)^{1/3} \frac{\Omega}{\omega}\right] \hat{\mathbf{e}}_{\parallel} + i\left(\frac{2}{n}\right)^{1/3} \text{Ai}'\left[-\left(\frac{2}{n}\right)^{1/3} \frac{\Omega}{\omega}\right] \hat{\mathbf{e}}_{\perp} \right\}, \quad (\text{A17})$$

where

$$C_{\varphi_0} = \frac{\sin[(n + m - \Omega/\omega)\pi]}{n + m - \Omega/\omega} + \frac{\sin[(n - m - \Omega/\omega)\pi]}{n - m - \Omega/\omega} \quad (\text{A18})$$

is the factor resulting from the integration over  $\varphi_0$ . This series has an infinite number of non-zero terms because, on the one hand, the variable  $\varphi_0$  that labels the elements of the ring can only range over an interval of length  $2\pi$ , and on the other hand, the function  $\mathbf{B}^{\text{point}}$  that we are Fourier analyzing has different values at opposite ends of such an interval [see Section 2 of Ardavan et al. (2003)].

When  $\Omega/\omega$  is an integer, only the two terms  $n = \pm m + \Omega/\omega$  of the series in equation (A17) are non-zero: the numerators and denominators of the two fractions in equation (A18) simultaneously vanish approaching the limits  $\pi$ . But when  $\Omega/\omega$  is nonintegral, this series diverges, as expected from the fact that the singularity of the time-domain expression for  $\mathbf{B}^{\text{point}}$  in equation (A9) is non-integrable. There is a radical difference between the series in equation (A17) and its subluminal counterpart. Not only is it not possible to derive the frequency-domain expression for  $\mathbf{B}^{\text{ring}}$  by directly Fourier analyzing the time-domain expression for this field [which is divergent when the distance between the observer and the source decreases with the speed  $dR_0/dt = -c$ ], but, correspondingly, the transformation  $t \rightarrow t + R_0(t)/c$  that takes one from the frequency-domain expression to the time-domain expression has a vanishing Jacobian and so is mathematically impermissible in the superluminal case. a25

On the one hand, each source element  $\varphi_0$  of the ring makes its contribution towards the observed field at the discrete set of retarded times  $\omega t = \varphi_P - \varphi_0 + 3\pi/2 + 2k\pi$  at which it approaches the observer with the speed of light and zero acceleration, i.e. *periodically* with the period  $2\pi/\omega$ . On the other hand, temporal modulations of the density of the source occur on a time scale  $2\pi/\Omega$  that is incommensurable with the period  $2\pi/\omega$ . Because the emission time of the element labelled by  $\varphi_0$  is fixed (via  $\omega t = \varphi_P - \varphi_0 + 3\pi/2 + 2k\pi$ ) by its initial azimuthal position ( $\varphi_0$ ), the temporal  $[\exp(i\Omega t)]$  and spatial  $[\cos(m\varphi_0)]$  modulations of this source effectively combine into a single variation  $[\propto \exp(i\Omega\varphi_0/\omega) \cos(m\varphi_0)]$ . It is the Fourier decomposition of this variation with  $\varphi_0$ , or equivalently with the retarded time  $t$ , that together with the incommensurability of the two periods ( $2\pi/\omega$  and  $2\pi/\Omega$ ), and the finiteness of the domain of definition of  $\varphi_0$ , results in a spectrum containing all frequencies [see Fig. 5 of Ardavan et al. (2003)].

## A2 Radiation field of the entire volume of the source

In this Subsection, we use a similar procedure to find the field generated by the volume-distributed source described in equation (3) for which

$$\mathbf{j} = \frac{\partial \mathbf{P}}{\partial t} = \frac{1}{4} \text{is}(r, z) \sum_{\pm} (\Omega \pm m\omega) \exp[i(\Omega t \mp m\varphi_0)] + \{m \rightarrow -m, \Omega \rightarrow -\Omega\}, \quad (\text{A19})$$

where the symbol  $\{m \rightarrow -m, \Omega \rightarrow -\Omega\}$  designates a term exactly like the one preceding it but in which  $m$  and  $\Omega$  are everywhere replaced by  $-m$  and  $-\Omega$ , respectively. Here, we have replaced  $\hat{\varphi}$  by  $\varphi_0$  to bring out the connection with the ring source considered in Subsection A1.

Taking the curl of the first member of equation (A3) and discarding terms of order  $R^{-2}$ , we obtain the following

generalization of equation (A14):

$$\begin{aligned} \mathbf{B} &\simeq \frac{1}{c^2} \int r dr d\varphi dz dt \frac{\delta'(t - t_P + R/c)}{R} \hat{\mathbf{n}} \times \mathbf{j} \\ &= -\frac{i\omega^2}{2\pi c^2} \sum_{-\infty}^{\infty} n \exp(in\omega t_P) \int r dr d\varphi_0 dz dt R_0^{-1} \\ &\quad \times \exp[-in(\omega t + \hat{R}_0)] \hat{\mathbf{n}} \times \mathbf{j}, \end{aligned} \quad (\text{A20})$$

where

$$R_0 = [(z_P - z)^2 + r_P^2 + r^2 - 2rr_P \cos(\varphi_P - \varphi_0 - \omega t)]^{1/2}, \quad (\text{A21})$$

as before. Note that the change of integration variable from  $\varphi$  to  $\varphi_0 = \varphi - \omega t$  in the second member of this equation, that is made to emphasize the correspondence between equations (A14) and (A20), has a non-zero Jacobian and so is perfectly permissible.

For  $n \gg 1$  and a far-field observer outside the plane of rotation, i.e.  $\theta_P \neq \pi/2$ , the phase  $t + R_0(t)/c$  of the rapidly oscillating exponential in equation (A20) is stationary at  $t = t_c$ ,  $r = c \csc \theta_P$ , simultaneously, where  $\omega t_c = \varphi_P - \varphi_0 + 3\pi/2 + 2k\pi$  as in Subsection A1. Performing the integration with respect to these two variables by the method of stationary phase, we obtain the following expression for the electric field  $\mathbf{E} = -\hat{\mathbf{n}} \times \mathbf{B}$  of the radiation:

$$\mathbf{E} = \Re \left\{ \tilde{\mathbf{E}}_0 + 2 \sum_{n=1}^{\infty} \tilde{\mathbf{E}}_n \exp(-in\hat{\varphi}_P) \right\}, \quad (\text{A22})$$

in which

$$\begin{aligned} \tilde{\mathbf{E}}_n &\simeq \frac{m - \Omega/\omega}{2\hat{r}_P} \left(\frac{n}{2}\right)^{2/3} \exp \{i[n(\hat{R}_P + 3\pi/2) \\ &\quad - (\Omega/\omega)(\varphi_P + 3\pi/2)]\} K_r \mathbf{V} |_{\hat{r} = c \csc \theta_P} \\ &\quad \times \int_{-\pi}^{\pi} d\varphi_0 \exp[i(n - m + \Omega/\omega)\varphi_0] \\ &\quad + \{m \rightarrow -m, \Omega \rightarrow -\Omega\}, \end{aligned} \quad (\text{A23})$$

with

$$K_r \simeq \hat{r}_> - \hat{r}_<, \quad n \ll \pi \hat{R}_P / (\hat{r}_> - \hat{r}_<)^2, \quad (\text{A24})$$

or

$$K_r \simeq (2\pi \hat{R}_P / n)^{1/2} \exp(-i\pi/4), \quad n \gg \pi \hat{R}_P / (\hat{r}_> - \hat{r}_<)^2, \quad (\text{A25})$$

$$\begin{aligned} \mathbf{V} &= [\bar{s}_r \hat{\mathbf{e}}_{\parallel} + (\bar{s}_\varphi \cos \theta_P - \bar{s}_z \sin \theta_P) \hat{\mathbf{e}}_{\perp}] \\ &\quad \times \text{Ai} \left[ -\left(\frac{2}{n}\right)^{1/3} \frac{\Omega}{\omega} \right] - i(\bar{s}_\varphi \hat{\mathbf{e}}_{\parallel} - \bar{s}_r \cos \theta_P \hat{\mathbf{e}}_{\perp}) \\ &\quad \times \left(\frac{2}{n}\right)^{1/3} \text{Ai}' \left[ -\left(\frac{2}{n}\right)^{1/3} \frac{\Omega}{\omega} \right], \end{aligned} \quad (\text{A26})$$

and

$$\bar{s}_{r,\varphi,z} \equiv \int_{-\infty}^{\infty} dz \exp(in\hat{z} \cos \theta_P) s_{r,\varphi,z} |_{\hat{r} = c \csc \theta_P}. \quad (\text{A27})$$

Here,  $\Re$  stands for the real part of the quantity inside brackets,  $s_{r,\varphi,z}$  are the cylindrical components of  $\mathbf{s}$ , and  $\hat{r}_<$  and  $\hat{r}_>$  denote the radial boundaries of the superluminal part of the source that contributes towards the radiation at  $P$  (Ardavan et al. 2003).

As in the case of the ring source, the fact that the radiation observed at the time  $t_P$  is determined almost exclusively by the state of the emitting current at the retarded

time  $t = t_c$  turns the temporal modulation  $\exp(i\Omega t)$  of the source into a spatial modulation  $\exp(-i\Omega\varphi_0/\omega)$ . Consequently, the remaining integral in equation (A23) again has a non-zero value for all  $n$  when  $\Omega/\omega$  differs from an integer. Insertion of the resulting expression for  $\tilde{\mathbf{E}}_n$  in  $dP_n/d\Omega_P = cR_P^2|\tilde{\mathbf{E}}_n|^2/(2\pi)$  now yields the radiated power per harmonic per unit solid angle:

$$\frac{dP_n}{d\Omega_n} \simeq \frac{c^3}{2\pi\omega^2} \csc^2 \theta_P |K_r|^2 K_{\varphi_0}^2 \left(\frac{n}{2}\right)^{4/3} |\mathbf{V}|^2, \quad (\text{A28})$$

where

$$K_{\varphi_0} = (-1)^{n+m} \sin\left(\frac{\pi\Omega}{\omega}\right) \left(\frac{\mu_+}{n-\mu_+} + \frac{\mu_-}{n-\mu_-}\right), \quad (\text{A29})$$

and  $\mu_{\pm} = \pm m + \Omega/\omega$ . Since the Airy functions in equation (A26) decay exponentially with  $n$  when their argument is positive (Abramowitz & Stegun 1970), the terms associated with  $-\Omega < 0$  are ignored in the above expression.<sup>2</sup>

Evaluating the absolute value of the complex vector  $\mathbf{V}$  in equation (A26), we obtain

$$\begin{aligned} \frac{dP_n}{d\Omega_P} \propto & S_1(n)^2 \text{Ai}^2 \left[ -\left(\frac{2}{n}\right)^{1/3} \frac{\Omega}{\omega} \right] \\ & + S_2(n)^2 \left(\frac{2}{n}\right)^{2/3} \text{Ai}'^2 \left[ -\left(\frac{2}{n}\right)^{1/3} \frac{\Omega}{\omega} \right] \\ & + 2S_3(n)^2 \left(\frac{2}{n}\right)^{1/3} \text{Ai} \left[ -\left(\frac{2}{n}\right)^{1/3} \frac{\Omega}{\omega} \right] \\ & \times \text{Ai}' \left[ -\left(\frac{2}{n}\right)^{1/3} \frac{\Omega}{\omega} \right], \end{aligned} \quad (\text{A30})$$

in which

$$S_1(n) = n^{2/3} |K_r| K_{\varphi_0} \left( |\bar{s}_r|^2 + |\bar{s}_\varphi \cos \theta_P - \bar{s}_z \sin \theta_P|^2 \right)^{1/2}, \quad (\text{A31})$$

$$S_2(n) = n^{2/3} |K_r| K_{\varphi_0} \left( |\bar{s}_\varphi|^2 + |\bar{s}_r|^2 \cos^2 \theta_P \right)^{1/2}, \quad (\text{A32})$$

and

$$S_3(n) = n^{2/3} |K_r| K_{\varphi_0} \left\{ \Im [\bar{s}_r^* \cos \theta_P (\bar{s}_\varphi \cos \theta_P - \bar{s}_z \sin \theta_P) - \bar{s}_r \bar{s}_\varphi^*] \right\}^{1/2}. \quad (\text{A33})$$

Here,  $\Im$  and the superscript star denote the imaginary part and the conjugate of a complex variable, respectively.

<sup>2</sup> This expression for  $dP_n/d\Omega_P$  slightly differs from that derived in Ardavan et al. (2003) because, here, we have eliminated the usual step of integrating the first member of equation (A20) by parts to transfer the differentiation with respect to  $t$  from the delta function onto  $\mathbf{j}$ . Though making no difference in the subluminal case, this alternative procedure has the effect, in the superluminal case, of removing a multiplicative factor  $\mu_{\pm}$  from  $K_{\varphi_0}$  and instead multiplying the expression for  $\tilde{\mathbf{E}}_n$  by  $n$ .